A Novel 6G ISAC Channel Model Combining Forward and Backward Scattering

Runruo Yang, *Student Member, IEEE*, Cheng-Xiang Wang, *Fellow, IEEE*, Jie Huang, *Member, IEEE*, El-Hadi M. Aggoune, *Life Senior Member, IEEE*, and Yang Hao, *Fellow, IEEE*

***Abstract*— The integrated sensing and communication (ISAC) refers to the integration of radio sensing and wireless communications to realize the multiplexing of space, time, and frequency resources. In the sixth generation (6G) wireless networks, ISAC is considered as one of the most promising technologies. In this paper, a novel ISAC channel model combining forward and backward scattering is proposed. In addition to the non-stationarity caused by motions, the correlations between sensing and communication channels are investigated. The channel characteristics of sensing such as forward scattering and backward scattering are introduced into the communication channel model. Utilizing the correlations between sensing and communication channels, the communication channel model is divided into line-of-sight (LOS), forward scattering, and backward scattering components. These three components are summed according to probability weighting to obtain a more accurate channel model for sensing assisted communication systems. Moreover, important statistical properties of the proposed ISAC channel model are derived and simulated. The analytical and simulation results match well, demonstrating the correctness of derivations and simulations. Some derived/simulated statistical properties are verified by corresponding measurement data, which indicates the utility of the proposed ISAC channel model.**

***Index Terms*— 6G, ISAC channel model, non-stationary, forward scattering, backward scattering.**

Manuscript received 25 June 2022; revised 9 November 2022 and 20 January 2023; accepted 1 March 2023. Date of publication 22 March 2023; date of current version 13 November 2023. This work was supported in part by the National Key Research and Development Program of China under Grant 2018YFB1801101, in part by the National Natural Science Foundation of China (NSFC) under Grant 61960206006 and Grant 62271147, in part by the Key Technologies Research and Development Program of Jiangsu (Prospective and Key Technologies for Industry) under Grant BE2022067 and Grant BE2022067-1, in part by the EU Research and Innovation Staff Exchange (RISE) project under Horizon2020 Testing and Evaluating Sophisticated information and communication Technologies for enaBling scalablE smart griD Deployment (TESTBED2) Project under Grant 872172, in part by the High Level Innovation and Entrepreneurial Doctor Introduction Program in Jiangsu under Grant JSSCBS20210082, and in part by the University of Tabuk of Saudi Arabia under Grant 1444-154. The associate editor coordinating the review of this article and approving it for publication was W. Ni. *(Corresponding authors: Cheng-Xiang Wang; Jie Huang.)*

Runruo Yang, Cheng-Xiang Wang, and Jie Huang are with the National Mobile Communications Research Laboratory, School of Information Science and Engineering, Southeast University, Nanjing 210096, China, and also with the Purple Mountain Laboratories, Nanjing 211111, China (e-mail: ang_rr@seu.edu.cn; chxwang@seu.edu.cn; j_huang@seu.edu.cn).

El-Hadi M. Aggoune is with the Sensor Networks and Cellular Systems Research Center, University of Tabuk, Tabuk 47315, Saudi Arabia (e-mail: haggoune.sncs@ut.edu.sa).

Yang Hao is with the School of Electronic Engineering and Computer Science, Queen Mary University of London, E1 4NS London, U.K. (e-mail: y.hao@qmul.ac.uk).

Color versions of one or more figures in this article are available at https://doi.org/10.1109/TWC.2023.3258150.

Digital Object Identifier 10.1109/TWC.2023.3258150

I. Introduction

WITH the rapid development of wireless communication technologies, the fifth generation (5G) communication networks have been deployed and commercialized worldwide. The research on the sixth generation (6G) wireless networks has started with more requirements. For example, it can be used to map between the virtual and physical worlds, and further realize the intelligence and automation of the system [1], [2], [3]. In order to meet requirements of 6G, the wireless system needs to implement accurate sensing and wide coverage communication in the same system [4], [5], [6], [7], [8], [9]. With the demand of higher data rate, wireless communication systems need to deploy higher frequency bands [10], [11], [12], [13], which may overlap with the frequency bands traditionally used by radar systems [14], [15], [16]. In addition, wireless communication and sensing are similar in hardware, signal processing, and network architecture aspects [17], [18], [19], [20]. The similarities of these two systems provide the possibility for the emergence of integrated sensing and communication (ISAC) technologies. ISAC refers to the integration of communication and radio sensing to realize the multiplexing of time-frequency and space resources [21]. The purpose of ISAC is to achieve high-precision sensing while communicating with high quality, and the mutual benefit between the two functions will thus be realized [22], [23].

Most of the existing studies on ISAC systems have been focused on the transmission waveform or frame structure design, beamforming, and signal processing algorithms. The research on these aspects of ISAC system were carried out in [24], [25], [26], [27], [28], [29], and [30]. The authors in [24] used the method of minimizing the lower bound of joint delay and Doppler estimation to optimise orthogonal frequency-division multiplexing (OFDM) waveform, and both mono-static sensing and communication sub-systems were considered. Sensing information of the target can be represented by a two-way attenuation constant, delay, and Doppler shift of the target. For the communication subsystem, only a brief description was given in the paper, which considered the attenuation, delay, and Doppler shift of the paths, other than the correlation between these two subsystems. In [25], a beamforming method for ISAC multiple-input multiple-output (MIMO) system was formulated. The communication channels of different users were considered to be independent of each other. The mono-static sensing channels were divided into point target and extended target channels, wherein the extended target channel was composed of the summation of many point targets. In [26], an integrated system model of millimeter wave (mmWave) vehicle-to-vehicle (V2V) communication and radar based on IEEE 802.11ad was proposed. Both sensing and communication channels were modeled. The communication channel model was a time-invariant frequency-flat Rician channel, while the radar channel using the time- and frequency-selective model. The waveform design of mmWave ISAC system was studied in [27], including the radar-centric, communication-centric, and joint-coding cases. The channel models for communication and sensing were also considered. The communication channel was modeled as a line-of-sight (LOS) channel with delay taps, and the radar channel was modeled as time- and frequency-selective after exploiting beamforming at transmitter (Tx) and receiver (Rx) sides. In [28] and [29], the method of beam training, beam tracking, and beam prediction for vehicular network combining both radar and communication functions were investigated. A mono-static sensing subsystem model, including radar cross section (RCS), round-trip path loss, round-trip delay, and Doppler frequency. A communication subsystem model, represented by beamformer and steering vectors, was considered. Simulation results showed that the performance of sensing and communication can both be improved by beamforming method. In [30], a waveform optimization method was proposed to improve the mutual information of the ISAC system. The communication channel was assumed to be flat fading with coefficients following Gaussian distributions. The radar channel model was composed of RCS and Doppler shift. However, the above studies lack of details on the channel model. Meanwhile, one of the most important research scenarios for the ISAC system is vehicle-to-everything (V2X) [15], [31], [32], [33], which requires further studies of channel model and characteristics.

On the other hand, V2X communication channel models were studied in [34], [35], [36], [37], [38], and [12]. The authors in [12] proposed a 6G pervasive channel model (6GPCM), which can support all-spectrum, full-application scenarios, and global coverage scenarios. The non-stationarity caused by the motion of Tx, Rx, and clusters was considered in the 6GPCM. The authors in [34] proposed a non-stationary wideband MIMO channel model supporting the V2X scenario, in which the mobile terminal and clusters can move at arbitrary velocities and directions. A general three-dimensional (3D) non-stationary 5G geometry-based stochastic model (GBSM) was proposed in [35], where V2V, high-speed train (HST), and massive MIMO were considered in the channel model. In [36], a WINNER+ based 3D non-stationary wideband MIMO GBSM was proposed, in which the movements of Rx and clusters were considered, and the channel model was supported with measurements. In [37], a non-stationary geometry-based scattering V2V MIMO channel model was proposed. In [38], a novel 3D non-stationary GBSM was proposed, V2V, HST, massive MIMO, and mmWave-terahertz (THz) were considered, and verified by measurement data. However, current studies on channel model do not take the sensing function into account. A novel ISAC channel model shall be developed to simultaneously include both communication and sensing channels. In addition to considering the non-stationary feature of the communication channel itself, characteristics of the sensing channel such as forward scattering and backward scattering [39] are also required to be introduced. Sensing can be divided into forward scattering sensing and backward scattering sensing. Forward scattering refers to those with the scattering angle less than 90° relative to the incident direction of electromagnetic wave. Otherwise, referred to as backward scattering. In other words, the scatterers detected by a mono-static sensing channel can all be considered as backward scattering. In this paper, we use the mono-static sensing method, in which the backscatter sensing is used to obtain the information of the scatterer, such as the distances, angles, and motion parameters to improve the communication channel model. Utilizing the correlation between the sensing and the communication channels, a more precise communication channel model within the ISAC system can be established.

As far as the authors are aware, a channel model that considers both sensing and communication functions as well as their correlation has not been proposed before in the literature. A novel 6G ISAC channel model combining both forward and backward scattering is hence proposed and investigated for the first time in this paper. The main novelties and contributions of the paper are listed as follows.

1) A novel 6G ISAC channel model combining forward and backward scattering is first proposed. The proposed ISAC channel model with an improved accuracy consists of two parts, i.e., a sensing channel model and a communication channel model. The non-stationarity in the time domain caused by the movements of clusters and Rx is considered in the proposed model as well.
2) Different from other models, the communication channel model within the proposed ISAC channel model includes both forward scattering and backward scattering components in its non-line-of-sight (NLOS) paths. The two components are first multiplied/weighted by their probabilities and then summed to obtain the NLOS paths.
3) Statistical properties of the proposed ISAC channel model are investigated, including spatial cross-correlation function (CCF), temporal autocorrelation function (ACF), local temporal-Doppler power spectral density (PSD), local Doppler spread, root mean square delay spread (RMS DS), stationary distance, and coherence bandwidth. To illustrate the validity of the proposed channel model, we will compare measurements with simulation data.

The remainder of this paper is organized as follows. The novel 6G ISAC channel model combining forward and backward scattering is proposed in Section II. Section III derives the essential statistical properties of the theoretical channel model. Results and analysis of channel statistics are presented in Section IV. Finally, conclusions are drawn in Section V.

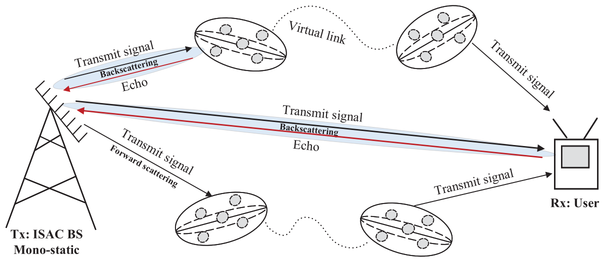

Fig. 1. The ISAC system model.

II. A Novel 6G ISAC GBSM

A novel 6G ISAC GBSM is proposed in this section. The ISAC system model is shown in Fig. 1. Tx is an ISAC base station (BS), and it can perform as a mono-static system realizing the signals transmission and backward scattering echo sensing signals reception. The ISAC BS serves the Rx, which can move with arbitrary velocity and trajectory, and the Rx is regarded as not only the sensing target but also the mobile user. The geometrical diagram of the ISAC channel model is presented in Fig. 2. The transmitting antenna array of ISAC BS is composed of M_T antennas, the antenna elements are equally spaced as δ^T. The transmit antenna array can be used to transmit sensing signals and communication signals at different time instants. The M_R^S equally spaced δ_S^R receiving antennas are used to receive the sensing echo signals. For the convenience of calculation, we assume that the transmit and receive arrays of the ISAC BS are both uniform linear arrays (ULAs). Rx side is the communication terminal (also the sensing target), which is also equipped with a ULA composed of M_R^C antenna elements with equal spacing δ_C^R. In addition to transmit and receive antenna arrays, the most important components in the channel model are clusters and rays. Each ray can be characterized by the distance, azimuth angle of departure (AAoD), elevation angle of departure (EAoD), azimuth angle of arrival (AAoA), and elevation angle of arrival (EAoA) parameters. The motion of the cluster can be described by speed and travel angles. In both sensing and communication subsystems, we have uniformly specified and described these parameters, which will be explained in details.

For the sensing system, the pth ($p = 1, \ldots, M_T$) transmit antenna element and the uth ($u = 1, \ldots, M_R^S$) receive antenna element of ISAC BS are A_p^T and A_u^{Rs}, respectively. The azimuth angle of the ISAC BS transmitting (receiving) antenna array can be represented as $\beta_A^{T(Rs)}$ in the $x-y$ plane, and $\beta_E^{T(Rs)}$ is the elevation angle of ISA BS transmitting (receiving) antenna array relative to $x-y$ plane. Symbol C_l denotes the cluster which can be sensed of the lth ($l = 1, \ldots, N_{up}^s(t)$) path, and it can also be seen as a part of surroundings sensing. The total number of paths between A_p^T and A_u^{Rs} at time t can be represented as $N_{up}^s(t)$. A cluster is the collection of scatterers with similar azimuth angles, elevation angles, and distances relative to the ISAC BS (or the Rx). The total number of scatterers in C_l is K_l. Symbols $v_0(t)$ and $v_l(t)$ represent the radial speeds relative to ISAC BS of Rx and C_l at time instant t, respectively. The travel azimuth angle and elevation angle of C_l are $\alpha_A^l(t)$ and $\alpha_E^l(t)$, respectively. AAoD and EAoD of the kth ($k = 1, \ldots, K_l$) ray in C_l transmitted from A_1^T at initial time can be expressed as θ_{A,k_l}, θ_{E,k_l}. Note that the transmitting and receiving arrays of ISAC BS are very close to each other, so we can consider the AAoD and EAoD are equal to AAoA and EAoA impinging on A_1^{Rs} at initial time, respectively. Similarly, we assume that AAoD and EAoD of the path from transmit array of ISAC BS to sensing target Rx are equal to AAoA and EAoA of the echo path from Rx to receiving array of ISAC BS. Therefore, the AAoD (AAoA) of path between ISAC BS and Rx and EAoD (EAoA) can be indicated as $\theta_{A,L}$ and $\theta_{E,L}$, respectively. D_0 is the distance from ISAC BS to Rx at initial time, and $d_{l,k}$ is the distance from A_1^T to C_l via the kth ray.

For the communication system, since it shares the same transmitting array with the sensing system, the pth transmit antenna element at ISAC BS and the qth ($q = 1, \ldots, M_R^C$) receive antenna element at Rx are A_p^T and A_q^{Rc}, respectively. The azimuth and elevation angles of Rx are β_A^{Rc} and β_E^{Rc}, respectively. In the communication channel model, it is assumed that there are multi-bounces between Tx and Rx. For the forward scattering component, the nth ($n = 1, \ldots, N_{qp}^c(t)$) path between A_p^T and A_q^{Rc} can be expressed as the sum of A_p^T to the first-bounce cluster C_n^A, the last-bounce cluster C_n^Z to A_q^{Rc}, and the virtual link between C_n^A and C_n^Z. The total number of paths between A_p^T and A_q^{Rc} is $N_{qp}^c(t)$. Similarly, the first-bounce cluster and the last-bounce cluster of the lth ($l = 1, \ldots, N_{qp}^s(t)$) path of backward scattering component are C_l^A and C_l^Z, respectively. It can be assumed that $N_{qp}^s(t) = N_{up}^s(t)$. For the forward scattering and backward scattering components, the distributions of clusters are random in space and do not conform to any specific geometric distribution. The speeds of the Rx, $C_{n(l)}^A$, and $C_{n(l)}^Z$ relative to ISAC BS are $v^R(t)$, $v^{A_{n(l)}}(t)$, and $v^{Z_{n(l)}}(t)$, respectively. The travel azimuth (elevation) angles of Rx, C_n^A, C_n^Z, C_l^A, and C_l^Z are denoted by $\alpha_{A(E)}^R(t)$, $\alpha_{A(E)}^{A_n}(t)$, $\alpha_{A(E)}^{Z_n}(t)$, $\alpha_{A(E)}^{A_l}(t)$, and $\alpha_{A(E)}^{Z_l}(t)$, respectively. The AAoD (EAoD) of the mth ($m = 1, \ldots, M_n$) ray in C_n^A and the kth ($k = 1, \ldots, K_l$) ray in C_l^A transmitted from A_1^T at initial time are $\phi_{A(E),m_n}^T$ and $\phi_{A(E),k_l}^T$, respectively. Symbols M_n and K_l represent the total number of rays in C_n^A of forward scattering component and the total number of rays in C_l^A of backward scattering component, respectively. After that, symbols ϕ_{A,m_n}^R (ϕ_{A,k_l}^R) and ϕ_{E,m_n}^R (ϕ_{E,k_l}^R) are the AAoA and EAoA of the mth (kth) ray in C_n^Z (C_l^Z) impinging on A_1^{Rc} at initial time, respectively. For the forward scattering component, the distance from A_1^T (A_1^{Rc}) to C_n^A (C_n^Z) via the mth ray at initial time can be denoted by $d_{m_n}^{T(R)}$. The distance from A_p^T (A_q^{Rc}) to C_n^A (C_n^Z) via the mth ray at time instant t is denoted as $d_{p,m_n}^T(t)$ ($d_{q,m_n}^R(t)$). Similarly, for the backward scattering component, the distance from A_1^T (A_1^{Rc}) to C_l^A (C_l^Z) via the kth ray at initial time can be denoted by $d_{k_l}^{T(R)}$. The distance from A_p^T (A_q^{Rc}) to C_l^A (C_l^Z) via the kth ray at time instant t is denoted as $d_{p,k_l}^T(t)$ ($d_{q,k_l}^R(t)$). The AAoD, EAoD, AAoA, and EAoA of the LOS path at initial time are denoted as $\phi_{A,L}^T$, $\phi_{E,L}^T$, $\phi_{A,L}^R$, and $\phi_{E,L}^R$, respectively.

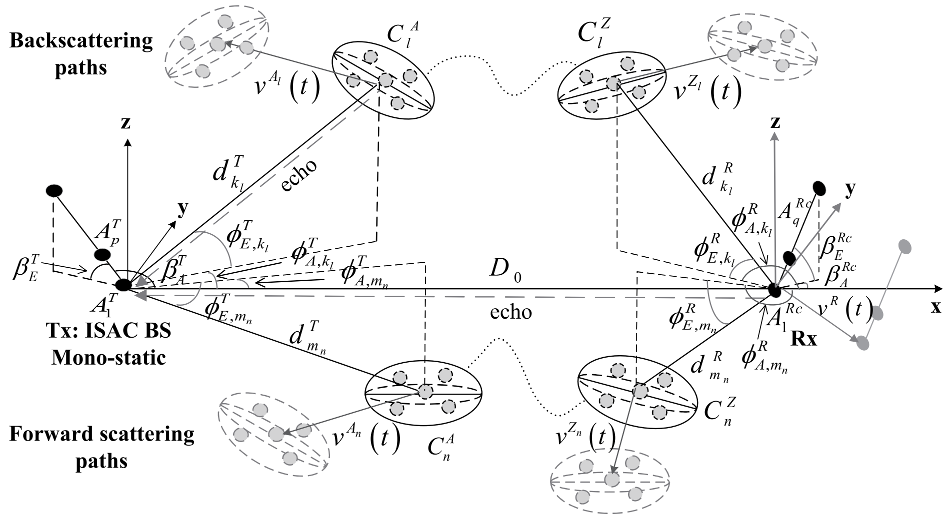

Fig. 2. The ISAC channel model including LOS path, forward scattering paths, and backward scattering paths.

TABLE I
DEFINITIONS OF MAIN PARAMETERS OF SENSING CHANNEL

Parameters	Definitions
A_p^T, A_u^{Rs}	The pth transmit antenna element, the uth receive antenna element of ISAC BS
δ^T, δ_S^R	Antenna spacings of transmit and receive antenna arrays of ISAC BS
$\beta_A^{T(Rs)}$, $\beta_E^{T(Rs)}$	Azimuth and elevation angles of the transmit and receive antenna arrays of ISAC BS
C_l	The cluster which can be sensed of the lth path
$v_0(t)$, $v_l(t)$	Radial speeds relative to ISAC BS of Rx and C_l, respectively
$\alpha_A^l(t)$, $\alpha_E^l(t)$	Travel azimuth angle and elevation angle of C_l, respectively
θ_{A,k_l}, θ_{E,k_l}	AAoD (AAoA) and EAoD (EAoA) of the kth ray in C_l transmitted from A_1^T (impinging on A_1^{Rs}) at initial time, respectively
$\theta_{A,L}$, $\theta_{E,L}$	AAoD (AAoA) and EAoD (EAoA) of the echo path between ISAC BS and Rx
D_0	Distance from ISAC BS $A_1^T$to Rx A_1^{Rc} at initial time
$d_{l,k}$	Distance from A_1^T to C_l via the kth ray

The distance from ISAC BS A_1^T to Rx A_1^{Rc} is D_0 at initial time, and the distance from ISAC BS A_p^T to Rx A_q^{Rc} is $D_{qp}(t)$ at time instant t. For convenience, the important parameters of sensing and communication channel models mentioned above are summarized in Table I and Table II, respectively.

The ISAC channel model needs to be divided into two parts, i.e., the sensing channel model and the communication channel model. The main difference between sensing channel and communication channel is that in the former, there are only LOS paths between ISAC BS and sensing objects. For the communication channel, there are both LOS paths and NLOS paths between ISAC BS and Rx. However, there are still certain correlations between the sensing channel and communication channel. The novel ISAC channel model proposed in this paper utilizes the correlations between sensing and communication, and reflects how the sensing assists the communication channel modeling. In practical application, for the communication with relatively long duration. It is necessary to obtain parameters from the sensing channel time and again during the communication process to ensure the accuracy of the communication channel model. The sensing channel should be modeled at the beginning to obtain the distances, angles, and motion parameters of the communication user and clusters in the environment, and these parameters are used to model the initial communication channel. Then the channel information can be sensed again after the time interval ΔT_s, and the communication channel can be updated with the newly sensed parameters. To cycle this process and obtain the channel of the whole communication period. For the reason that the above process is a repeat of the same operation, that is, to obtain the sensing information at first and then assist the communication channel modeling by obtained parameters of the sensing channel. We will describe in detail the sensing channel modeling and how to use the sensing information to model the communication channel at the initial time. The channel impulse responses (CIRs) of sensing channel and communication channel will be introduced in the next two subsections, respectively.

A. Sensing CIR

In the (radar) sensing system, scattering can be divided into forward scattering and backward scattering, on the basis of the type of material used on the surface of the scatterers and the difference of roughness. For the mono-static sensing system which is used in this paper, only backward scattering can provide the required sensing information, and only the

TABLE II
DEFINITIONS OF MAIN PARAMETERS OF COMMUNICATION CHANNEL

Parameters	Definitions
A_p^T, A_q^{Rc}	The pth ISAC BS transmit antenna element and the qth Rx receive antenna element
δ^T, δ_C^R	Antenna spacings of transmit array of ISAC BS and receive array of Rx
β_A^{Rc}, β_E^{Rc}	Azimuth and elevation angles of the receive array of Rx
C_n^A (C_l^A), C_n^Z (C_l^Z)	The first- and last-bounce clusters of the nth (lth) path of forward (backward) scattering components
$v^R(t)$, $v^{A_n}(t)$ ($v^{A_l}(t)$), $v^{Z_n}(t)$ ($v^{Z_l}(t)$)	Speeds of the Rx, C_n^A (C_l^A) and C_n^Z (C_l^Z), respectively
$\alpha_{A/E}^R(t)$, $\alpha_{A/E}^{A_n}(t)$ ($\alpha_{A/E}^{A_l}(t)$), $\alpha_{A/E}^{Z_n}(t)$ ($\alpha_{A/E}^{Z_l}(t)$)	Travel azimuth/elevation angles of Rx, C_n^A (C_l^A) and C_n^Z (C_l^Z), respectively
ϕ_{A,m_n}^T (ϕ_{A,k_l}^T), ϕ_{E,m_n}^T (ϕ_{E,k_l}^T)	AAoD and EAoD of the mth (kth) ray in C_n^A (C_l^A) transmitted from A_1^T at initial time, respectively
ϕ_{A,m_n}^R (ϕ_{A,k_l}^R), ϕ_{E,m_n}^R (ϕ_{E,k_l}^R)	AAoA and EAoA of the mth (kth) ray of forward (backward) scattering components in C_n^Z (C_l^Z) impinging on A_1^{Rc} at initial time, respectively
$\phi_{A,L}^T$, $\phi_{E,L}^T$	AAoD and EAoD of the LOS path transmitted from A_1^T at initial time, respectively
$\phi_{A,L}^R$, $\phi_{E,L}^R$	AAoA and EAoA of the LOS path impinging on A_1^R at initial time, respectively
$d_{m_n}^T$ ($d_{k_l}^T$), $d_{m_n}^R$ ($d_{k_l}^R$)	Distance from A_1^T to C_n^A (C_l^A) and distance from A_1^{Rc} to C_n^Z (C_l^Z) via the mth (kth) ray of forward (backward) scattering components at initial time, respectively
$d_{p,m_n}^T(t)$ ($d_{p,k_l}^T(t)$), $d_{q,m_n}^R(t)$ ($d_{q,k_l}^R(t)$)	Distance from A_p^T to C_n^A (C_l^A) and distance from A_q^{Rc} to C_n^Z (C_l^Z) via the mth (kth) ray of forward (backward) scattering components at time instant t, respectively
D_0	Distance from ISAC BS A_1^T to Rx A_1^{Rc} at initial time
$D_{qp}(t)$	Distance from ISAC BS A_p^T to Rx A_q^{Rc} at time instant t

backward scattering part is considered in the sensing CIR. The sensing CIR can be divided into two parts, i.e., communication terminal target sensing echo CIR and scatterers sensing echo CIR in the environment, which are expressed as the first and second terms to the right of (1). The sensing CIR can be denoted as

$$\begin{aligned} h^{rad}(t,\tau) = & \sqrt{G_0} e^{j2\pi f_{D0}(t)t} e^{j2\pi f_c \tau_0} A_{rad}(\theta_{A,L},\theta_{E,L}) \\ & \times \delta(\tau-\tau_0) + \sum_{l=1}^{N_{up}^s(t)-1} \sum_{k=1}^{K_l} \sqrt{G_{l,k}} e^{j2\pi f_{Dl}(t)t} \\ & \times e^{j2\pi f_c \tau_{l,k}} A_{rad}(\theta_{A,k_l},\theta_{E,k_l}) \cdot \delta(\tau-\tau_{l,k}) \end{aligned} \quad (1)$$

where f_c is carrier frequency, $G_0 = \lambda^2 \sigma_{RCS,0} / \left(64\pi^3 D_0^4\right)$ represents the large-scale channel gain between ISAC BS and sensing target in radar system, and λ is the wavelength, $\sigma_{RCS,0}$ is the RCS of sensing target, D_0 is the distance between ISAC BS and sensing target at initial time. Similarly, $G_{l,k} = \lambda^2 \sigma_{RCS,l,k} / \left(64\pi^3 d_{l,k}^4\right)$ represents the large-scale channel gain between ISAC BS and the kth scatterer in C_l, $\sigma_{RCS,l,k}$ is RCS of the kth scatterer, $d_{l,k}$ is the distance between ISAC BS and the kth scatterer. Symbols $\tau_0 = 2D_0/c$ and $\tau_{l,k} = 2d_{l,k}/c$ are delays of the echo paths scattered by sensing target and the kth scatterer, where c is the speed of light. Doppler shift of the echo paths scattered by sensing target and the cluster are $f_{D0}(t) = 2v_0(t)/\lambda$ and $f_{Dl}(t) = 2v_l(t)/\lambda$, respectively. It is important to note that the distances of the echo paths are twice of distance between ISAC BS and target or the scatterer. Symbols $A_{rad}(\theta_{A,L},\theta_{E,L})$ and $A_{rad}(\theta_{A,k_l},\theta_{E,k_l})$ denote the product of the steering vectors of transmit array and receive array of ISAC BS when it is used as target and environmental cluster sensing, respectively. The parameters which can be determined from the target sensing channel are the distance D_0, the delay τ_0, the radial velocity $v_0(t)$, and the AAoD (AAoA) and EAoD (EAoA) of echo path between Rx and ISAC BS, i.e., $\theta_{A,L}$ and $\theta_{E,L}$. The parameters which can be determined from the environmental cluster sensing channel are the total number of backward scattering clusters $N_{up}^s(t)$, which can be sensed by mono-static system, the distance $d_{l,k}$, radial velocity $v_l(t)$, and angle parameters θ_{A,k_l} (θ_{E,k_l}). Utilizing the information provided by sensing channel, a more precise communication channel model can be proposed.

B. Communication CIR

For the communication channel model, path loss PL, shadowing SH, and small-scale fading should be considered. The complex channel matrix can be denoted by $\mathbf{H} = [PL \cdot SH]^{\frac{1}{2}} \mathbf{H}_s$, where $\mathbf{H}_s = \left[h_{qp}^{com}(t,\tau)\right]_{M_R^C \times M_T}$ is complex channel matrix of small-scale fading, and $h_{qp}^{com}(t,\tau)$ is communication CIR between A_p^T and A_q^{Rc}. The communication channel model proposed in this paper needs to be divided into LOS and NLOS paths. On account of the addition of sensing system, the NLOS paths are divided into forward scattering paths and backward scattering paths. The mono-static sensing system can only distinguish the scatterers which are backward scattered, but the two kinds of scatterers are both existing in communication channel model. For the purpose of making the channel model proposed in this paper more general, it can be reasonably assumed that the power transmitting for NLOS component are departed into two parts, forward scattering power and backward scattering power. The ratio of this two parts power can be represented by the probabilities. The forward scattering components include scatterers that cannot be sensed. The parameters, such as angles, distances, and velocities, of these scatterers should be randomly generated. The backward scattering components include all scatterers that can be sensed by the sensing channel, and the parameters of these scatterers can be provided directly by sensing system. Since the LOS path is necessary between the sensing object and the ISAC BS, for the paths with multi-bounce clusters, only the information of the first-bounce clusters of communication channel model on the ISAC BS side can be sensed. So that the first-bounce clusters' information of the backward scattering paths in communication channel model can be provided by the sensing. If the LOS path between ISAC BS and Rx exists, the position and motion parameters of Rx can also be determined by the sensing channel. This also indicates the correlation between the sensing channel and the communication channel.

The communication CIR $h_{qp}^{com}(t,\tau)$ can be obtained by adding LOS, forward scattering, and backward scattering parts in the way of probability weighted summation, and $h_{qp}^{com}(t,\tau)$ can be calculated as

$$\begin{aligned} &h_{qp}^{com}(t,\tau) \\ &= p_L(t)\cdot\sqrt{\frac{K}{K+1}}h_{qp}^{L}(t,\tau) \\ &\quad+\sqrt{\frac{1}{K+1}}\left(p_N^f(t)\cdot h_{qp}^{Nf}(t,\tau)+p_N^b(t)\cdot h_{qp}^{Nb}(t,\tau)\right) \end{aligned} \tag{2}$$

where $p_L(t)$, $p_N^f(t)$, and $p_N^b(t)$ are the probabilities of LOS, forward scattering, and backward scattering components, respectively, and K is Rician factor. For the probability of LOS component, in the outdoor urban macro (UMa) scenario, it can be denoted as [41]

$$\begin{aligned} &p_L(t) \\ &=\begin{cases} 1, & D_0\le 18\text{ m} \\ \left[\frac{18}{D_0}+\left(1-\frac{18}{D_0}\right)\exp\left(-\frac{D_0}{63}\right)\right] \\ \cdot\left[1+C'(h_{UE})\frac{5}{4}\left(\frac{D_0}{100}\right)^3\right. \\ \qquad\left.\cdot\exp\left(-\frac{D_0}{150}\right)\right], & D_0>18\text{ m} \end{cases} \end{aligned} \tag{3}$$

where h_{UE} is the height of communication terminal, and

$$C'(h_{UE})=\begin{cases} 0, & h_{UE}\le 13\text{ m} \\ \left(\frac{h_{UE}-13}{10}\right)^{1.5}, & 13\text{ m}<\mathrm{h_{UE}}\le 23\text{ m}. \end{cases} \tag{4}$$

The probabilities of forward and backward scattering components can be expressed as the proportion of forward scattering and backward scattering paths to the total number of paths, which are formulated as

$$p_N^f(t)=\frac{N_{qp}^c(t)M_n}{N_{qp}^c(t)M_n+N_{qp}^s(t)K_l} \tag{5}$$

$$p_N^b(t)=\frac{N_{qp}^s(t)K_l}{N_{qp}^c(t)M_n+N_{qp}^s(t)K_l}. \tag{6}$$

The CIR of LOS component in (2) can be denoted as

$$\begin{aligned} h_{qp}^{L}(t,\tau)=&\begin{bmatrix} F_{q,V}\left(\phi_{E,L}^R,\phi_{A,L}^R\right) \\ F_{q,H}\left(\phi_{E,L}^R,\phi_{A,L}^R\right)\end{bmatrix}^T\begin{bmatrix} e^{j\eta_L^{VV}} & 0 \\ 0 & -e^{j\eta_L^{HH}}\end{bmatrix} \\ &\cdot\begin{bmatrix} F_{p,V}\left(\phi_{E,L}^T,\phi_{A,L}^T\right) \\ F_{p,H}\left(\phi_{E,L}^T,\phi_{A,L}^T\right)\end{bmatrix}e^{j2\pi f_c\tau_{qp}^L(t)}\cdot\delta\left(\tau-\tau_{qp}^L(t)\right) \end{aligned} \tag{7}$$

where $\{\cdot\}^T$ means transposition, $F_{p,V(H)}$ and $F_{q,V(H)}$ denote the vertical (horizontal) polarization of antennas A_p^T and A_q^{Rc}, respectively, η_L^{VV} and η_L^{HH} are the initial phases uniformly distributed between $(0,2\pi]$, $\tau_{qp}^L(t)$ is the delay of LOS path between A_p^T and A_q^{Rc} at time t. The delay $\tau_{qp}^L(t)$ can be calculated by the following formula as

$$\tau_{qp}^L(t)=D_{qp}^c(t)/c \tag{8}$$

where $D_{qp}^c(t)=\left\|\vec{D}_{qp}^c(t)\right\|$ is the distance between A_p^T and A_q^{Rc}. It should be reminded that the sensing accuracy of the sensing system is determined by many factors, including the bandwidth and the size of antenna array. Therefore, without losing generality, there are reasons to assume that the first antenna element A_1^{Rc} of Rx can be sensed by the sensing system. The vector $\vec{D}_{qp}^c(t)$ can be written as

$$\vec{D}_{qp}^c(t)=\vec{D}+\vec{l}_q^{Rc}-\vec{l}_p^T+\int_0^t\vec{v}^R(t)\,dt \tag{9}$$

where $\vec{D}=[D_0,0,0]$, the value of D_0 can be provided by sensing, $\vec{l}_p^T$ and $\vec{l}_q^{Rc}$ are antenna position vectors, i.e., the vectors from A_1^T to A_p^T and A_1^{Rc} to A_q^{Rc}. The antenna position vectors can be written as

$$\vec{l}_p^T=\delta_p^T\left[\cos\left(\beta_E^T\right)\cos\left(\beta_A^T\right),\cos\left(\beta_E^T\right)\sin\left(\beta_A^T\right),\sin\left(\beta_E^T\right)\right] \tag{10}$$

$$\vec{l}_q^{Rc}=\delta_q^{Rc}\left[\cos\left(\beta_E^{Rc}\right)\cos\left(\beta_A^{Rc}\right),\cos\left(\beta_E^{Rc}\right)\sin\left(\beta_A^{Rc}\right),\sin\left(\beta_E^{Rc}\right)\right] \tag{11}$$

where δ_p^T is the distance between A_1^T and A_p^T, and δ_q^{Rc} is the distance between A_1^{Rc} and A_q^{Rc}. They can be denoted as $\delta_p^T=(p-1)\,\delta^T$, $\delta_q^{Rc}=(q-1)\,\delta_C^R$. Note that the radial velocity vector $\vec{v}^R(t)$ can be determined by sensing system, where the radial velocity is $v^R(t)=v_0(t)$, and the travel angles of Rx are equal to the angles of transmit beams of sensing system, $\phi_{A,L}^T=\theta_{A,L}$ and $\phi_{E,L}^T=\theta_{E,L}$. Therefore, the vector $\vec{v}^R(t)$ can be calculated as

$$\begin{aligned} \vec{v}^R(t)=&v^R(t)\left[\cos\left(\phi_{E,L}^T\right)\cos\left(\phi_{A,L}^T\right),\cos\left(\phi_{E,L}^T\right)\sin\left(\phi_{A,L}^T\right),\right. \\ &\left.\sin\left(\phi_{E,L}^T\right)\right] \\ =&v_0(t)\left[\cos\left(\theta_{E,L}\right)\cos\left(\theta_{A,L}\right),\cos\left(\theta_{E,L}\right)\sin\left(\theta_{A,L}\right),\right. \\ &\left.\sin\left(\theta_{E,L}\right)\right]. \end{aligned} \tag{12}$$

The distance $D_{qp}^c(t)$ can be solved by

$$\begin{aligned} &\left|D_{qp}^c(t)\right|^2 \\ &=\left[D_0-\cos\left(\beta_A^T\right)\cos\left(\beta_E^T\right)\delta_p^T\right. \\ &\quad\left.+\cos\left(\beta_A^{Rc}\right)\cos\left(\beta_E^{Rc}\right)\delta_q^{Rc}+\cos\left(\theta_{E,L}\right)\cos\left(\theta_{A,L}\right)v_0t\right]^2 \end{aligned}$$

$$+\left[\cos\left(\beta_E^{Rc}\right)\sin\left(\beta_A^{Rc}\right)\delta_q^{Rc}-\cos\left(\beta_E^{T}\right)\sin\left(\beta_A^{T}\right)\delta_p^{T}\right.$$
$$\left.+\cos\left(\theta_{E,L}\right)\sin\left(\theta_{A,L}\right)v_0t\right]^2+\left[\sin\left(\beta_E^{T}\right)\delta_p^{T}\right.$$
$$\left.-\sin\left(\beta_E^{Rc}\right)\delta_q^{Rc}+\sin\left(\theta_{E,L}\right)v_0t\right]^2. \quad (13)$$

The forward scattering components CIR $h_{qp}^{Nf}(t,\tau)$ in (2) can be determined as

$$\begin{aligned} &h_{qp}^{Nf}(t,\tau)\\ &=\sum_{n=1}^{N_{qp}^{c}(t)}\sum_{m=1}^{M_n}\begin{bmatrix}F_{q,V}\left(\phi_{E,m_n}^R,\phi_{A,m_n}^R\right)\\ F_{q,H}\left(\phi_{E,m_n}^R,\phi_{A,m_n}^R\right)\end{bmatrix}^T\\ &\cdot\begin{bmatrix}e^{j\eta_{m_n}^{VV}} & \sqrt{\kappa_{m_n}^{-1}}e^{j\eta_{m_n}^{VH}}\\ \sqrt{\kappa_{m_n}^{-1}}e^{j\eta_{m_n}^{HV}} & e^{j\eta_{m_n}^{HH}}\end{bmatrix}\begin{bmatrix}F_{p,V}\left(\phi_{E,m_n}^T,\phi_{A,m_n}^T\right)\\ F_{p,H}\left(\phi_{E,m_n}^T,\phi_{A,m_n}^T\right)\end{bmatrix}\\ &\cdot\sqrt{P_{qp,m_n}(t)}e^{j2\pi f_c\tau_{qp,m_n}(t)}\delta\left(\tau-\tau_{qp,m_n}(t)\right) \end{aligned} \quad (14)$$

where $\eta_{m_n}^{VV}$, $\eta_{m_n}^{VH}$, $\eta_{m_n}^{HV}$, and $\eta_{m_n}^{HH}$ are uniformly distributed random phases over (0,2π], κ_{m_n} is the cross polarization power ratio, $P_{qp,m_n}(t)$ and $\tau_{qp,m_n}(t)$ represent the power and time delay of mth ray in nth path at time instant t, respectively. The delay $\tau_{qp,m_n}(t)$ can be determined by

$$\tau_{qp,m_n}(t)=d_{qp,m_n}(t)/c+\tilde{\tau}_{m_n} \quad (15)$$

where $\tilde{\tau}_{m_n}$ means the delay of virtual link between $S_{m_n}^A$ and $S_{m_n}^Z$, $S_{m_n}^A$ and $S_{m_n}^Z$ are the mth scatterers in C_n^A and C_n^Z, respectively. The virtual delay can be calculated as $\tilde{\tau}_{m_n}=\tilde{d}_{m_n}\big/c+\tau'$, where $\tilde{d}_{m_n}$ is the distance between $S_{m_n}^A$ and $S_{m_n}^Z$, τ' is the delay of multi bounces between $S_{m_n}^A$ and $S_{m_n}^Z$, and τ' is an exponentially distributed non-negative random variable [40]. The distance $d_{qp,m_n}(t)$ is determined by

$$d_{qp,m_n}(t)=\left\|\vec{d}_{p,m_n}^T(t)\right\|+\left\|\vec{d}_{q,m_n}^R(t)\right\| \quad (16)$$

where $\vec{d}_{p,m_n}^T(t)$ and $\vec{d}_{q,m_n}^R(t)$ are given by

$$\vec{d}_{p,m_n}^T(t)=\vec{d}_{m_n}^T-\vec{l}_p^T+\int_0^t\vec{v}^{A_n}(t)\,dt \quad (17)$$

$$\vec{d}_{q,m_n}^R(t)=\vec{d}_{m_n}^R-\left[\vec{l}_q^{Rc}+\int_0^t\vec{v}^R(t)-\vec{v}^{Z_n}(t)\,dt\right]. \quad (18)$$

The vectors $\vec{d}_{m_n}^{T(R)}$, $\vec{v}^{A_n}$ and $\vec{v}^{Z_n}$ can be calculated as

$$\begin{aligned}\vec{d}_{m_n}^{T(R)}=d_{m_n}^{T(R)}&\left[\cos\left(\phi_{E,m_n}^{T(R)}\right)\cos\left(\phi_{A,m_n}^{T(R)}\right),\right.\\ &\left.\cos\left(\phi_{E,m_n}^{T(R)}\right)\sin\left(\phi_{A,m_n}^{T(R)}\right),\sin\left(\phi_{E,m_n}^{T(R)}\right)\right]\end{aligned} \quad (19)$$

$$\begin{aligned}\vec{v}^{A_n}(t)=v^{A_n}(t)&\left[\cos\left(\alpha_E^{A_n}(t)\right)\cos\left(\alpha_A^{A_n}(t)\right),\right.\\ &\left.\cos\left(\alpha_E^{A_n}(t)\right)\sin\left(\alpha_A^{A_n}(t)\right),\sin\left(\alpha_E^{A_n}(t)\right)\right]\end{aligned} \quad (20)$$

$$\begin{aligned}\vec{v}^{Z_n}(t)=v^{Z_n}(t)&\left[\cos\left(\alpha_E^{Z_n}(t)\right)\cos\left(\alpha_A^{Z_n}(t)\right),\right.\\ &\left.\cos\left(\alpha_E^{Z_n}(t)\right)\sin\left(\alpha_A^{Z_n}(t)\right),\sin\left(\alpha_E^{Z_n}(t)\right)\right].\end{aligned} \quad (21)$$

The power $P_{qp,m_n}(t)$ can be calculated as [41]

$$P'_{qp,m_n}(t)=\exp\left(-\tau_{qp,m_n}(t)\frac{r_\tau-1}{r_\tau DS}\right)10^{-\frac{Z_n}{10}} \quad (22)$$

where r_τ is the delay distribution proportionality factor, DS is delay spread, and Z_n is the per cluster shadowing term. After normalization, it can be written as

$$P_{qp,m_n}(t)=P'_{qp,m_n}(t)\bigg/\sum_{n=1}^{N_{qp}^c(t)}\sum_{m=1}^{M_n}P'_{qp,m_n}(t). \quad (23)$$

If the delays of multipath components within the cluster cannot be distinguished, the formula (22) can be simplified as

$$P'_{qp,m_n}(t)=\frac{1}{M_n}\exp\left(-\tau_{qp,n}(t)\frac{r_\tau-1}{r_\tau DS}\right)10^{-\frac{Z_n}{10}}. \quad (24)$$

In the equations, the distance and angle parameters between the scatterers and Tx or Rx can be determined by the ellipsoid Gaussian scattering model [38]. In ellipsoid Gaussian scattering model, (x_1,y_1,z_1) represent the coordinates of clusterer in global coordinate system, and it can be modeled as

$$f(x_1,y_1,z_1)=\frac{\exp\left(-\frac{x_1^2}{2\varepsilon_{DS}^2}-\frac{y_1^2}{2\varepsilon_{AS}^2}-\frac{z_1^2}{2\varepsilon_{ES}^2}\right)}{(2\pi)^{3/2}\varepsilon_{DS}\varepsilon_{AS}\varepsilon_{ES}} \quad (25)$$

where ε_{DS}, ε_{AS}, and ε_{ES} are the delay spread, azimuth angle spread, and elevation angle spread of the cluster, respectively. They all follow the standard derivations of the Gaussian distributions. When the spherical coordinates of the cluster center in global coordinate system are (d,ϕ_E,ϕ_A), taking the cluster center as the origin, the local coordinates of the scatterer can be written as (x,y,z), and the relationship with (x_1,y_1,z_1) is written as

$$\begin{aligned}\begin{bmatrix}x\\y\\z\end{bmatrix}&=\begin{bmatrix}\cos(\phi_A) & -\sin(\phi_A) & 0\\ \sin(\phi_A) & \cos(\phi_A) & 0\\ 0 & 0 & 1\end{bmatrix}\\ &\cdot\begin{bmatrix}\cos(\phi_E) & 0 & -\sin(\phi_E)\\ 0 & 1 & 0\\ \sin(\phi_E) & 0 & \cos(\phi_E)\end{bmatrix}\begin{bmatrix}x_1-d\\ y_1\\ z_1\end{bmatrix}.\end{aligned} \quad (26)$$

The angle parameters ϕ_{A,m_n}^T (ϕ_{A,m_n}^R), $\phi_{E,m_n}^T(\phi_{E,m_n}^R)$, and the distance $d_{m_n}^T(d_{m_n}^R)$ can be calculated by substituting $x=d_{m_n}^{T(R)}\cos\left(\phi_{E,m_n}^{T(R)}\right)\cos\left(\phi_{A,m_n}^{T(R)}\right)$, $y=d_{m_n}^{T(R)}\cos\left(\phi_{E,m_n}^{T(R)}\right)\sin\left(\phi_{A,m_n}^{T(R)}\right)$, and $z=d_{m_n}^{T(R)}\sin\left(\phi_{E,m_n}^{T(R)}\right)$ into (26).

The backward scattering components CIR $h_{qp}^{Nb}(t,\tau)$ in (2) can be determined as

$$\begin{aligned} &h_{qp}^{Nb}(t,\tau)\\ &=\sum_{l=1}^{N_{qp}^{s}(t)}\sum_{k=1}^{K_l}\begin{bmatrix}F_{q,V}\left(\phi_{E,k_l}^R,\phi_{A,k_l}^R\right)\\ F_{q,H}\left(\phi_{E,k_l}^R,\phi_{A,k_l}^R\right)\end{bmatrix}^T\\ &\cdot\begin{bmatrix}e^{j\eta_{k_l}^{VV}} & \sqrt{\kappa_{k_l}^{-1}}e^{j\eta_{k_l}^{VH}}\\ \sqrt{\kappa_{k_l}^{-1}}e^{j\eta_{k_l}^{HV}} & e^{j\eta_{k_l}^{HH}}\end{bmatrix}\begin{bmatrix}F_{p,V}\left(\phi_{E,k_l}^T,\phi_{A,k_l}^T\right)\\ F_{p,H}\left(\phi_{E,k_l}^T,\phi_{A,k_l}^T\right)\end{bmatrix}\\ &\cdot\sqrt{P_{qp,k_l}(t)}e^{j2\pi f_c\tau_{qp,k_l}(t)}\delta\left(\tau-\tau_{qp,k_l}(t)\right) \end{aligned} \quad (27)$$

where AAoD and EAoD can be obtained by sensing channel $\phi_{A,k_l}^T=\theta_{A,k_l}$, $\phi_{E,k_l}^T=\theta_{E,k_l}$. The calculation of delay

$\tau_{qp,k_l}(t)$ is similar to that of forward scattering path and it can be given by

$$\tau_{qp,k_l}(t) = d_{qp,k_l}(t)/c + \tilde{\tau}_{k_l} \tag{28}$$

where $\tilde{\tau}_{k_l}$ is the virtual delay, and the $d_{qp,k_l}(t)$ can be calculated by

$$d_{qp,k_l}(t) = \left\| \vec{d}^{T}_{p,k_l}(t) \right\| + \left\| \vec{d}^{R}_{q,k_l}(t) \right\|. \tag{29}$$

It differs from forward scattering in that the information from the Tx to C_l^A can be completely determined by the sensing system, that is, the first term on the right of (29) is known. The vector $\vec{d}^{T}_{p,k_l}(t)$ can be calculated by

$$\vec{d}^{T}_{p,k_l}(t) = \vec{d}^{T}_{k_l} - \left[\vec{l}^{T}_{p} + \int_0^t \vec{v}^{A_l}(t)\, dt \right]. \tag{30}$$

The parameters of the paths between ISAC BS and C_l^A of backward scattering components, including the distance, AAoD, and EAoD of kth ray in C_l^A, can be determined by the sensing channel, i.e., $d^T_{k_l} = d_{l,k}$, $\phi^T_{A,k_l} = \theta_{A,k_l}$, and $\phi^T_{E,k_l} = \theta_{E,k_l}$. Therefore, $\vec{d}^{T}_{k_l}$ can be calculated as

$$\begin{aligned} \vec{d}^{T}_{k_l} &= d^T_{k_l} \left[\cos\left(\phi^T_{A,k_l}\right)\cos\left(\phi^T_{E,k_l}\right), \sin\left(\phi^T_{A,k_l}\right)\cos\left(\phi^T_{E,k_l}\right), \right. \\ &\qquad \left. \sin\left(\phi^T_{E,k_l}\right) \right] \\ &= d_{l,k} \left[\cos\left(\theta_{A,k_l}\right)\cos\left(\theta_{E,k_l}\right), \sin\left(\theta_{A,k_l}\right)\cos\left(\theta_{E,k_l}\right), \right. \\ &\qquad \left. \sin\left(\theta_{E,k_l}\right) \right]. \end{aligned} \tag{31}$$

The travel speed, azimuth and elevation angles of C_l^A are known as $v^{A_l}(t) = v_l(t)$, $\alpha^{A_l}_A(t) = \alpha^l_A(t)$, and $\alpha^{A_l}_E(t) = \alpha^l_E(t)$, respectively. Therefore, the vector $\vec{v}^{A_l}(t)$ can be calculated as

$$\begin{aligned} &\vec{v}^{A_l}(t) \\ &= v^{A_l}(t) \left[\cos\left(\alpha^{A_l}_A(t)\right)\cos\left(\alpha^{A_l}_E(t)\right), \right. \\ &\qquad \left. \sin\left(\alpha^{A_l}_A(t)\right)\cos\left(\alpha^{A_l}_E(t)\right), \sin\left(\alpha^{A_l}_E(t)\right) \right] \\ &= v_l(t) \left[\cos\left(\alpha^l_A(t)\right)\cos\left(\alpha^l_E(t)\right), \right. \\ &\qquad \left. \sin\left(\alpha^l_A(t)\right)\cos\left(\alpha^l_E(t)\right), \sin\left(\alpha^l_E(t)\right) \right]. \end{aligned} \tag{32}$$

The calculation method of $\vec{d}^{R}_{q,k_l}(t)$ is the same as that of forward scattering, i.e.,

$$\vec{d}^{R}_{q,k_l}(t) = \vec{d}^{R}_{k_l} - \left[\vec{l}^{Rc}_{q} + \int_0^t \vec{v}^{R}(t) - \vec{v}^{Z_l}(t)\, dt \right]. \tag{33}$$

The power $P_{qp,k_l}(t)$ can also be obtained by referring to (22)–(24).

For the GBSM without sensing assistance, the distance and angle parameters from Tx to the first-bounce cluster and the last-bounce cluster to Rx should be generated by the random generation method. The speed and travel angles of the cluster of the communication channel model should also be generated randomly. For the novel ISAC channel model proposed in this paper, the distance and angle parameters from Tx to Rx and to the first-bounce cluster can be directly provided by the sensing channel, so there is no need for random generation. Therefore, the complexity of the communication channel model is reduced to a certain extent. The parameters that can be provided by the sensing channel are summarized in Table III.

The transfer function of the communication channel model is written as

$$\begin{aligned} &H^{com}_{qp}(t,f) \\ &= p_L(t)\sqrt{\frac{K}{K+1}} H^L_{qp}(t,f) \\ &\quad + \sqrt{\frac{1}{K+1}} \left(p^f_N(t) H^{Nf}_{qp}(t,f) + p^b_N(t) H^{Nb}_{qp}(t,f) \right) \end{aligned} \tag{34}$$

where $H^L_{qp}(t,f)$, $H^{Nf}_{qp}(t,f)$, and $H^{Nb}_{qp}(t,f)$ are the transfer functions of LOS, forward scattering, and backward scattering components, respectively. These transfer functions are the Fourier transform of their CIRs, respectively. For the convenience of calculation, the antenna polarization is not included in the transfer functions, and the transfer functions can be denoted as

$$H^L_{qp}(t,f) = \exp\left[-j2\pi\tau^L_{qp}(t)(f-f_c)\right] \tag{35}$$

$$\begin{aligned} &H^{Nf}_{qp}(t,f) \\ &= \sum_{n=1}^{N^c_{qp}(t)} \sum_{m=1}^{M_n} \sqrt{P_{qp,m_n}(t)} \exp\left[-j2\pi\tau_{qp,m_n}(t)(f-f_c)\right] \end{aligned} \tag{36}$$

$$\begin{aligned} &H^{Nb}_{qp}(t,f) \\ &= \sum_{l=1}^{N^s_{qp}(t)} \sum_{k=1}^{K_l} \sqrt{P_{qp,k_l}(t)} \exp\left[-j2\pi\tau_{qp,k_l}(t)(f-f_c)\right]. \end{aligned} \tag{37}$$

III. STATISTICAL PROPERTIES

In this section, in order to verify that the proposed channel model can accurately describe the scatterer distributions and the channel is non-stationary in time domain for the outdoor scenario with moving clusters and user, some important statistical properties of the channel model are studied.

A. Local STF Correlation Function

The local space-time-frequency (STF) correlation function can be represented as

$$\begin{aligned} &R_{qp,\tilde{q}\tilde{p}}(t,f;\Delta r,\Delta t,\Delta f) \\ &\qquad = E\left\{ H^{com}_{qp}(t,f) H^{com*}_{\tilde{q}\tilde{p}}(t-\Delta t, f-\Delta f) \right\} \end{aligned} \tag{38}$$

where $E\{\cdot\}$ means expectation, $(\cdot)^*$ is the complex conjugation operation, Δr, Δt, and Δf are the antenna elements interval, time interval, and frequency interval, respectively. The antenna elements interval can be calculated as $\Delta r = \delta^T_{\tilde{p}} - \delta^T_p$ for the transmitter or $\Delta r = \delta^{Rc}_{\tilde{q}} - \delta^{Rc}_q$ for the receiver. The variables taken in the expectation of (38) are Δr, Δt, and Δf. The expectations of Δr, Δt, and Δf correspond to the temporal CCF, spatial ACF, and frequency correlation function (FCF), respectively. By substituting the transfer function in (34) into the right side of (38), a further STF correlation function can be obtained as the sum of correlation functions of

TABLE III

SENSING AIDED PARAMETERS FOR COMMUNICATION CHANNEL

Parameters	Definitions
$v^R(t) = v_0(t)$, $v^{A_l}(t) = v_l(t)$	Speeds of the Rx and C_l^A relative to ISAC BS, respectively
$\alpha_{A(E)}^{A_l}(t) = \alpha_{A(E)}^{l}(t)$	Travel azimuth (elevation) angle of C_l^A, respectively
$\phi_{A(E),k_l}^{T} = \theta_{A(E),k_l}$	AAoD (EAoD) of the kth ray in C_l^A transmitted from A_1^T at initial time, respectively
$\phi_{A(E),L}^{T} = \theta_{A(E),L}$	AAoD (EAoD) of the LOS path transmitted from A_1^T at initial time, respectively
$d_{k_l}^T = d_{l,k}$	Distance from A_1^T to C_l^A via the kth ray of backscattering components at initial time
D_0	Distance from ISAC BS A_1^T to Rx A_1^{Rc} at initial time

LOS, forward scattering, and backward scattering components, i.e.,

$$\begin{aligned} &R_{qp,\tilde{q}\tilde{p}}(t,f;\Delta r,\Delta t,\Delta f) \\ &= p_L(t)\frac{K}{K+1}R_{qp,\tilde{q}\tilde{p}}^{L}(t,f;\Delta r,\Delta t,\Delta f) \\ &\quad + \frac{1}{K+1}\left(p_N^f(t)\sum_{n=1}^{N_{qp}^c(t)}R_{qp,\tilde{q}\tilde{p},n}^{Nf}(t,f;\Delta r,\Delta t,\Delta f)\right. \\ &\quad\left. + p_N^b(t)\sum_{l=1}^{N_{qp}^s(t)}R_{qp,\tilde{q}\tilde{p},l}^{Nb}(t,f;\Delta r,\Delta t,\Delta f)\right). \end{aligned} \tag{39}$$

The STF correlation functions of LOS, forward scattering, and backward scattering components can be calculated by the transfer functions of these three components denoted in (35)–(37), respectively. The STF correlation function of LOS component is

$$\begin{aligned} &R_{qp,\tilde{q}\tilde{p}}^{L}(t,f;\Delta r,\Delta t,\Delta f) \\ &= E\left\{H_{qp}^{L}(t,f)\,H_{\tilde{q}\tilde{p}}^{L\,*}(t-\Delta t,f-\Delta f)\right\} \\ &= \left[P_{qp}^{L}(t)\,P_{\tilde{q}\tilde{p}}^{L}(t-\Delta t)\right]^{\frac{1}{2}} \\ &\quad\times e^{j\frac{2\pi(f_c-f)}{\lambda f_c}\left[D_{qp}(t)-D_{\tilde{q}\tilde{p}}(t-\Delta t)\right]-j\frac{2\pi\Delta f}{\lambda f_c}D_{\tilde{q}\tilde{p}}(t-\Delta t)}. \end{aligned} \tag{40}$$

The STF correlation function of forward scattering component is

$$\begin{aligned} &R_{qp,\tilde{q}\tilde{p}}^{Nf}(t,f;\Delta r,\Delta t) \\ &= E\left\{H_{qp}^{Nf}(t,f)\,H_{\tilde{q}\tilde{p}}^{Nf*}(t-\Delta t,f)\right\} \\ &= E\left\{\sum_{m=1}^{M_n}\left[P_{qp,m_n}(t)\,P_{\tilde{q}\tilde{p},m_n}(t-\Delta t)\right]^{\frac{1}{2}}\right. \\ &\quad\left.\times e^{j\frac{2\pi(f_c-f)}{\lambda f_c}\left[d_{qp,m_n}(t)-d_{\tilde{q}\tilde{p},m_n}(t-\Delta t)\right]-j\frac{2\pi\Delta f}{\lambda f_c}d_{\tilde{q}\tilde{p},m_n}(t-\Delta t)}\right\}. \end{aligned} \tag{41}$$

Finally, the STF correlation function of backward scattering component is

$$\begin{aligned} &R_{qp,\tilde{q}\tilde{p}}^{Nb}(t,f;\Delta r,\Delta t) \\ &= E\left\{H_{qp}^{Nb}(t,f)\,H_{\tilde{q}\tilde{p}}^{Nb*}(t-\Delta t,f)\right\} \\ &= E\left\{\sum_{k=1}^{K_l}\left[P_{qp,k_l}(t)\,P_{\tilde{q}\tilde{p},k_l}(t-\Delta t)\right]^{\frac{1}{2}}\right. \\ &\quad\left.\times e^{j\frac{2\pi(f_c-f)}{\lambda f_c}\left[d_{qp,k_l}(t)-d_{\tilde{q}\tilde{p},k_l}(t-\Delta t)\right]-j\frac{2\pi\Delta f}{\lambda f_c}d_{\tilde{q}\tilde{p},k_l}(t-\Delta t)}\right\}. \end{aligned} \tag{42}$$

If $\Delta t = 0$ and $\Delta f = 0$, the STF correlation function can be simplified to spatial CCF. Set $\Delta r = 0$ and $\Delta f = 0$ to acquire the temporal ACF. The FCF can be obtained by setting $\Delta r = 0$ and $\Delta t = 0$.

Therefore, the spatial CCF can be computed as

$$\begin{aligned} &R_{qp,\tilde{q}\tilde{p}}(t,f;\Delta r) \\ &= p_L(t)\cdot\frac{K}{K+1}R_{qp,\tilde{q}\tilde{p}}^{L}(t,f;\Delta r) \\ &\quad + \frac{1}{K+1}\cdot\left(p_N^f(t)\cdot\sum_{n=1}^{N_{qp}^c(t)}R_{qp,\tilde{q}\tilde{p},n}^{Nf}(t,f;\Delta r)\right. \\ &\quad\left. + p_N^b(t)\cdot\sum_{l=1}^{N_{qp}^s(t)}R_{qp,\tilde{q}\tilde{p},l}^{Nb}(t,f;\Delta r)\right). \end{aligned} \tag{43}$$

The spatial CCF is closely related to the distribution of scatterers, and it is an important statistical property to verify that the ISAC channel model can more accurately reflect the physical environment of the channel. Temporal ACF is the statistical property to verify time domain non-stationarity, and it can be computed as

$$\begin{aligned} &R_{qp}(t,f;\Delta t) \\ &= p_L(t)\cdot\frac{K}{K+1}R_{qp}^{L}(t,f;\Delta t) \\ &\quad + \frac{1}{K+1}\cdot\left(p_N^f(t)\cdot\sum_{n=1}^{N_{qp}^c(t)}R_{qp,n}^{Nf}(t,f;\Delta t)\right. \\ &\quad\left. + p_N^b(t)\cdot\sum_{l=1}^{N_{qp}^s(t)}R_{qp,l}^{Nb}(t,f;\Delta t)\right). \end{aligned} \tag{44}$$

The FCF is an important intermediate property for subsequent calculation of the coherent bandwidth, and it can be obtained as

$$\begin{aligned} &R_{qp}(t,f;\Delta f) \\ &= p_L(t)\cdot\frac{K}{K+1}R_{qp}^{L}(t,f;\Delta f) \\ &\quad + \frac{1}{K+1}\cdot\left(p_N^f(t)\cdot\sum_{n=1}^{N_{qp}^c(t)}R_{qp,n}^{Nf}(t,f;\Delta f)\right. \\ &\quad\left. + p_N^b(t)\cdot\sum_{l=1}^{N_{qp}^s(t)}R_{qp,l}^{Nb}(t,f;\Delta f)\right). \end{aligned} \tag{45}$$

B. Local Temporal-Doppler PSD

The local temporal-Doppler PSD $S_{qp}(t,f;\omega)$ can reflect the time domain non-stationary characteristic of the channel, and it can be derived by performing the Fourier transform on the temporal ACF $R_{qp}(t,f;\Delta t)$ as

$$S_{qp}(t,f;\omega) = \int R_{qp}(t,f;\Delta t) \cdot e^{-j2\pi\omega\Delta t} d(\Delta t) \tag{46}$$

where ω is Doppler frequency.

C. Local Doppler Spread

The movements of Rx or the scatterers in the environment will lead to time selectivity, which can be intuitively represented by local Doppler spread. The instantaneous Doppler frequency is obtained by the instantaneous frequency $\frac{d\Phi(t)}{2\pi dt}$ [42], where $\Phi(t)$ is the phase change and $\frac{d(\cdot)}{dt}$ means the differential operation with respect to time t. The phase changes of the NLOS paths propagating via the mth scatterer of the forward scattering component and the kth scatterer of the backward scattering component are denoted as $\Phi_{m_n}(t) = \frac{2\pi\left[d^T_{p,m_n}(t)+d^R_{q,m_n}(t)\right]}{\lambda}$ and $\Phi_{k_l}(t) = \frac{2\pi\left[d^T_{p,k_l}(t)+d^R_{q,k_l}(t)\right]}{\lambda}$, respectively. The instantaneous Doppler frequency is denoted as

$$\begin{aligned}\varpi_{qp}(t) &= p^f_N \cdot \varpi_{qp,m_n}(t) + p^b_N \cdot \varpi_{qp,k_l}(t) \\ &= p^f_N \cdot \frac{d\Phi_{m_n}(t)}{dt} + p^b_N \cdot \frac{d\Phi_{k_l}(t)}{dt} \\ &= \frac{1}{\lambda}\left[p^f_N \cdot \frac{d\left[d^T_{p,m_n}(t)+d^R_{q,m_n}(t)\right]}{dt}\right. \\ &\qquad \left. + p^b_N \cdot \frac{d\left[d^T_{p,k_l}(t)+d^R_{q,k_l}(t)\right]}{dt}\right]. \end{aligned} \tag{47}$$

Therefore, the local Doppler spread can be determined as

$$B_{qp}(t) = \sqrt{E\left[\varpi_{qp}(t)^2\right] - E^2[\varpi_{qp}(t)]}. \tag{48}$$

D. RMS DS

In the communication system, the signals are transmitted through different paths, resulting in multipath transmission. The signals reach the Rx at different time instants, further leading to frequency selectivity. The instantaneous RMS DS is the normalized second-order central moment describing the time-varying delay PSD. It can be assumed that the time-variant delay PSD of the jth ($j = 1, 2, \ldots, J$) path in forward scattering can be expressed as

$$PDP^f_j(t,\tau_j) = \left|h^{Nf}_{qp}(t,\tau_j)\right|^2. \tag{49}$$

Similarly, the delay PSD corresponding to the ith ($i = 1, 2, \ldots, I$) path in backward scattering components is

$$PDP^b_i(t,\tau_i) = \left|h^{Nb}_{qp}(t,\tau_i)\right|^2. \tag{50}$$

For ISAC channel model, the RMS DS of the channel can be denoted as

$$\tau_{rms} = p^f_N \cdot \tau^f_{rms} + p^b_N \cdot \tau^b_{rms} \tag{51}$$

where τ^f_{rms} and τ^b_{rms} represent RMS DS of forward scattering and backward scattering components, respectively. They can be calculated as

$$\tau^f_{rms} = \sqrt{\frac{\sum_{j=1}^{J}\left|h^{Nf}_{qp}(t,\tau_j)\right|^2 \cdot \tau_j^2}{\sum_{j=1}^{J}\left|h^{Nf}_{qp}(t,\tau_j)\right|^2}} \tag{52}$$

$$\tau^b_{rms} = \sqrt{\frac{\sum_{i=1}^{I}\left|h^{Nb}_{qp}(t,\tau_i)\right|^2 \cdot \tau_i^2}{\sum_{i=1}^{I}\left|h^{Nb}_{qp}(t,\tau_i)\right|^2}}. \tag{53}$$

E. Stationary Distance

In the real scenes, the Tx, Rx, and the scatterers between them are often moving, so the channel is considered to be non-stationary. The non-stationarity degree of the channel can be measured numerically by the stationary time interval $T_{st} = |t_k - t_j|$ [43], which is decided by the similarity of delay PSD at different times t_j and t_k. The stationary distance is the distance that Rx moves within the stationary interval, which can be calculated as $D_{st} = T_{st} \cdot v^R$ [44]. The correlation of delay PSD at time instant t_j and t_k can be denoted by

$$c(t_j,t_k) = p^f_N \cdot c^f(t_j,t_k) + p^b_N \cdot c^b(t_j,t_k) \tag{54}$$

where

$$c^f(t_j,t_k) = \frac{\int \left|h^{Nf}_{qp}(t_j,\tau)\right| \cdot \left|h^{Nf}_{qp}(t_k,\tau)\right| d\tau}{\max\left\{\int \left|h^{Nf}_{qp}(t_j,\tau)\right|^2 d\tau, \int \left|h^{Nf}_{qp}(t_k,\tau)\right|^2 d\tau\right\}} \tag{55}$$

$$c^b(t_j,t_k) = \frac{\int \left|h^{Nb}_{qp}(t_j,\tau)\right| \cdot \left|h^{Nb}_{qp}(t_k,\tau)\right| d\tau}{\max\left\{\int \left|h^{Nb}_{qp}(t_j,\tau)\right|^2 d\tau, \int \left|h^{Nb}_{qp}(t_k,\tau)\right|^2 d\tau\right\}}. \tag{56}$$

F. Coherence Bandwidth

Coherence bandwidth is a key statistical characteristic for measuring frequency selective fading caused by delay diffusion. When FCF is equal to a given threshold c_{th}, which can be determined according to the specific situation, the corresponding minimum frequency interval is the coherence bandwidth [45], i.e.,

$$f_{corr}(c_{th}) = \min\{\Delta f > 0 : R_{qp}(t,f;\Delta f) = c_{th}\} \tag{57}$$

where $\min\{\cdot\}$ denotes taking the minimum value.

IV. RESULTS AND ANALYSIS

In this section, the statistical characteristics of the ISAC channel model proposed in this paper are investigated. We compare the analytical results, simulation results, and measurement data of statistical characteristics to verify the practicability and accuracy of the proposed channel model. Here, the analytical results are obtained by plotting the mathematical derivation results of the corresponding statistical

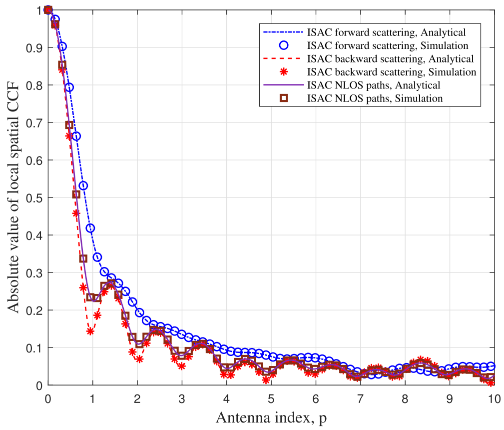

(a) Local spatial CCF with sparsely distributed clusters

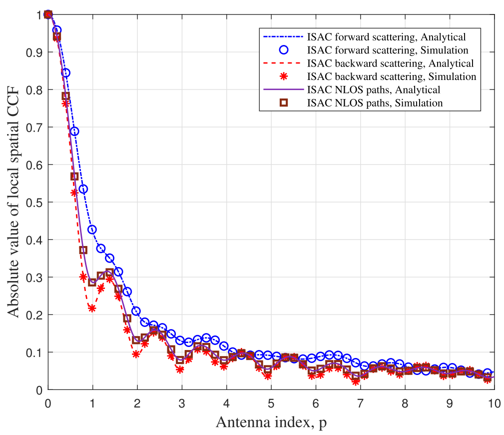

(b) Local spatial CCF with densely distributed clusters

Fig. 3. The comparison of local spatial CCFs of analytical results and simulation results for forward scattering, backward scattering, and NLOS paths with (a) sparsely distributed and (b) densely distributed clusters (f_c = 5.9 GHz, D = 100 m, M_T = 16, M_R^c = 4, $\delta^T = \delta_C^R = \lambda/2$, $\beta_A^T = \pi/4$, $\beta_E^T = \pi/10$, $\beta_A^R = \pi/4$, $\beta_E^R = \pi/10$, v^R = 10 m/s, $\alpha_A^R(t) = \alpha_E^R(t) = 0$, $v^{A_n}(t) = v^{A_l}(t) = v^{Z_n}(t) = v^{Z_l}(t)$ = 0 m/s, σ_A^R = 28.2°, σ_E^R = 13.5°, (a) σ_A^T = 47°, σ_E^T = 23.54°, (b) σ_A^T = 15.23°, σ_E^T = 10.1°).

properties, while the simulation results are obtained by Matlab simulations starting from the CIR in (2) or the Fourier transform of the CIR in (34).

A. Local Spatial CCF

The simulation results of local spatial CCFs for forward scattering components, backward scattering components, and NLOS components, which is consisted of forward and backward scattering, are given in Fig. 3. Fig. 3 shows the channel local spatial CCFs when the first-bounce clusters distribution is sparse and dense, the difference of these two conditions are represented by the variances of AAoD σ_A^T and EAoD σ_E^T. The variances of AAoA σ_A^R and EAoA σ_E^R are the same in both cases. The variance of angle can be calculated as $\sigma_{A(E)}^{T/R} =$

$$\sqrt{\frac{\sum\limits_{n=1}^{N_{qp}^c(t)}\sum\limits_{m=1}^{M_n}\left(\phi_{A(E),m_n}^{T/R}-\bar{\phi}_{A(E)}^{T/R}\right)^2+\sum\limits_{l=1}^{N_{qp}^s(t)}\sum\limits_{k=1}^{K_l}\left(\phi_{A(E),k_l}^{T/R}-\bar{\phi}_{A(E)}^{T/R}\right)^2}{N_{qp}^c(t)M_n+N_{qp}^s(t)K_l}},$$

where $\bar{\phi}_{A(E)}^{T/R}$ is the average of AAoD/AAoA (EAoD/EAoA) for all rays. The individual variance is used to describe the offset of the angle of rays relative to the average angle for all rays, and it also indicates the degree of angle dispersion of the clusters in the environment. It can be found that when the cluster distribution is dense, the local spatial CCFs are relatively large, while when the cluster distribution is sparse, the spatial CCFs are small. The local spatial CCF simulation results of backward scattering channel are more vulnerable to the change of clusters position compare to that of forward scattering channel. It is because that the position of the first-bounce cluster in backward scattering part is given by the sensing system, which is different from the randomly generated clusters position in forward scattering. The results also demonstrate that the backward scattering channel is more precise compared with the forward scattering channel. In addition, the simulation results are fairly aligned with the analytical results, which proves the validity of the channel model.

B. Local Temporal ACF

The local temporal ACFs of forward scattering, backward scattering, and NLOS components are provided in Fig. 4 at t = 0 s, t = 1 s, and t = 10 s, respectively. All of these local temporal ACFs are time-variant for the reasons of Rx and clusters movements. This illustrates the non-stationary in time domain of the channel model, that is, the parameters in the channel model are time-varying, and the wide-sense stationary (WSS) in time domain will no longer be applicable. The temporal ACFs at t = 0 s and t = 1 s are similar, because the time interval is small and the channel similarity is high. Due to the movements of Rx and clusters, the attenuation of temporal ACFs becomes more and more serious over time. Besides, the analytical results and simulation results are well aligned with each other, which proves the availability of the channel model.

C. Local Temporal-Doppler PSD

The simulated and analytical results of the time-variant temporal-Doppler PSD of forward scattering, backward scattering, and NLOS components are shown in Fig. 5 at times t = 0 s, t = 1 s, and t = 10 s, respectively. It can be found out that the temporal-Doppler PSD varies over time for all of these three components, that is because the non-stationary in time domain of the channel model proposed in the paper. The difference between Doppler PSD curves at times t = 0 s and t = 1 s is small, on account of the time interval is small and the non-stationary phenomenon is not obvious. The temporal-Doppler PSD gradually leveled over time, as a result of Rx and cluster motions. In addition, the simulation results show good approximation to the analytical results, which proves that the channel model is practical.

D. Local Doppler Spread

In Fig. 6, the simulated and analytical results for local Doppler spreads of the ISAC channel model are compared with

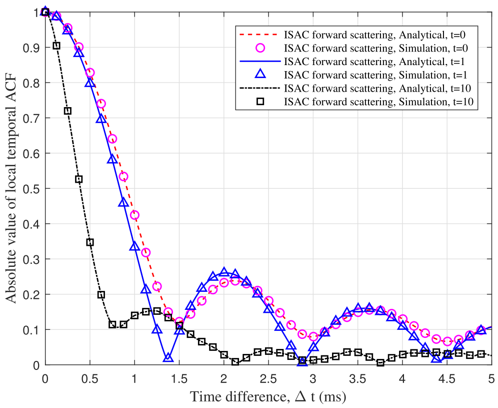

(a) Forward scattering components

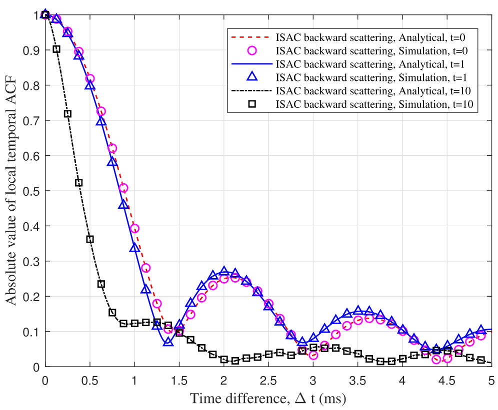

(b) Backward scattering components

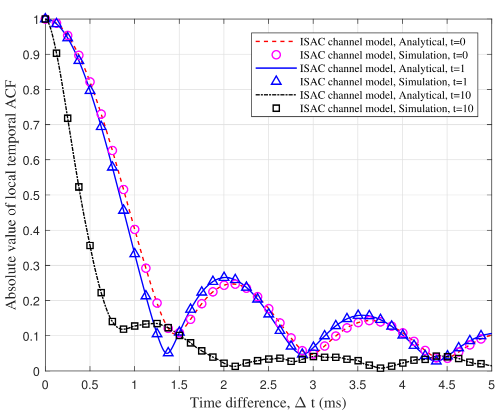

(c) NLOS components

Fig. 4. The analytical and simulated local temporal ACF of ISAC channel model at t = 0 s, t = 1 s, and t = 10 s for (a) backward scattering components, (b) forward scattering components, and (c) NLOS components (f_c = 5.9 GHz, D = 150 m, M_T = 16, M_R^c = 4, $\delta^T = \delta_C^R = \lambda/2$, $\beta_A^T = \pi/4$, $\beta_E^T = \pi/10$, $\beta_A^R = \pi/4$, $\beta_E^R = \pi/10$, v^R = 17 m/s, $\alpha_A^R(t) = \alpha_E^R(t) = 0$, $v^{A_n}(t) = v^{A_l}(t) = v^{Z_n}(t) = v^{Z_l}(t)$ = 0 m/s, σ_A^T = 30.6°, σ_E^T = 6.4°, σ_A^R = 52°, σ_E^R = 10.2°).

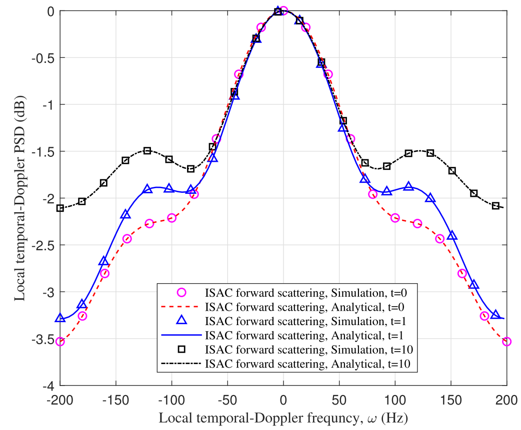

(a) Forward scattering components

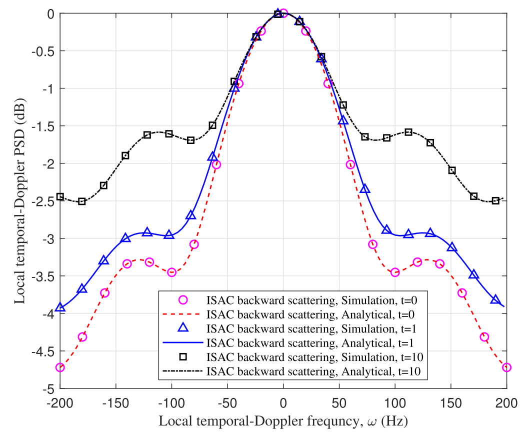

(b) Backward scattering components

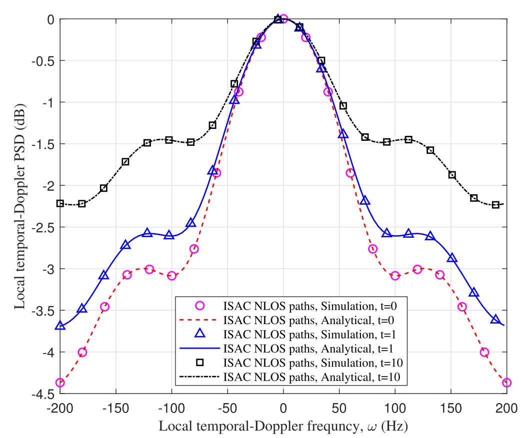

(c) NLOS components

Fig. 5. The analytical and simulated local temporal-Doppler PSD of ISAC channel model at t = 0 s, t = 1 s, and t = 10 s for (a) backward scattering components, (b) forward scattering components, and (c) NLOS components (f_c = 5.9 GHz, D = 150 m, M_T = 16, M_R^c = 4, $\delta^T = \delta_C^R = \lambda/2$, $\beta_A^T = \pi/4$, $\beta_E^T = \pi/10$, $\beta_A^R = \pi/4$, $\beta_E^R = \pi/10$, v^R = 10 m/s, $\alpha_A^R(t) = \pi/3$, $\alpha_E^R(t) = 0$, $v^{A_n}(t) = v^{A_l}(t) = v^{Z_n}(t) = v^{Z_l}(t)$ = 0 m/s, σ_A^T = 47°, σ_E^T = 23.5°, σ_A^R = 38.8°, σ_E^R = 38.2°).

corresponding measurement data in [46]. The measurement data was able to be obtained from the channel measurements which were carried out at 5.9 GHz in suburban scenario. The x-axis in Fig. 6 represents the speed of the Rx relative to that of the ISAC BS. We find that when v^R = 0, the local Doppler spread is not equal to zero, which is caused by the motion of clusters in the environment. Furthermore, the local Doppler spread simulation results of the proposed ISAC channel model

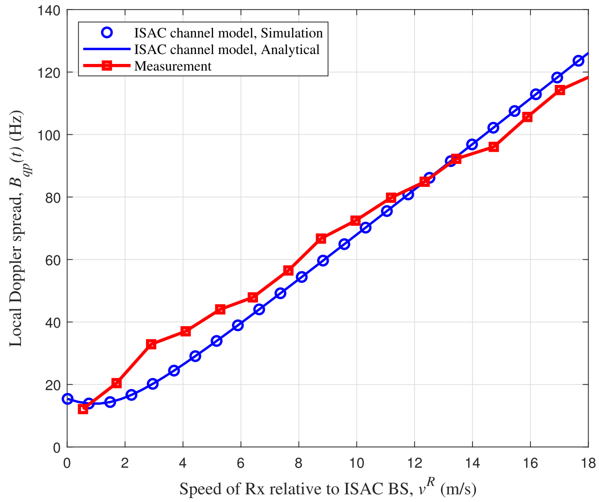

Fig. 6. The comparison of local Doppler spreads of the proposed ISAC channel model and measurement data in [46] (f_c = 5.9 GHz, D = 150 m, M_T = 4, M_R^c = 16, $\delta^T = \delta_C^R = \lambda/2$, $\beta_A^T = \pi/2$, $\beta_E^T = 0$, $\beta_A^R = \pi/2$, $\beta_E^R = 0$, $\alpha_A^R(t) = \pi/2$, $\alpha_E^R(t) = 0$, $v^{A_n}(t) = v^{A_l}(t) = v^{Z_n}(t) = v^{Z_l}(t) =$ 1 m/s, $\alpha_A^{A_n}(t) = \alpha_A^{A_l}(t) = \pi/2$, $\alpha_E^{A_n}(t) = \alpha_E^{A_l}(t) = 0$, $\alpha_A^{Z_n}(t) = \alpha_A^{Z_l}(t) = \pi/2$, $\alpha_E^{Z_n}(t) = \alpha_E^{Z_l}(t) = 0$, $\sigma_A^T = 27°$, $\sigma_E^T = 13.5°$, $\sigma_A^R = 8.8°$, $\sigma_E^R = 8.2°$).

and the measurement data are align well with each other, except for this, the simulation results can also agree very well with the analytical results.

E. RMS DS

In Fig. 7, the RMS DS simulation results of the proposed ISAC channel model are compared with the measurement data in [47]. The measurements were implemented in urban and suburban V2V scenarios at 5.9 GHz. The Tx and Rx are respectively placed on the roofs of the two vehicles, with a distance of 10 to 30 m. These two vehicles move in the same direction, and the velocities of both vehicles are maintained at about 40 km/h in urban scenario and 60 km/h in suburban scenario, respectively. Although there are other vehicles passing through, there is always the LOS path between Tx and Rx. It is revealed in Fig. 7 that the RMS DS simulation results of ISAC channel model can fit the measurement results well, whether in urban or suburban scenarios, and this demonstrates the validity and accuracy of the proposed ISAC channel model.

F. Stationary Distance

The stationary distance comparison between the simulation results of ISAC channel model and corresponding measurement data in [48] is shown in Fig. 8. In [48], the measurement campaigns were carried out in a typical urban V2V scenario at 5.9 GHz. The Tx and Rx are respectively located on the roofs of the two vehicles, Rx is located 100 meters behind Tx, and the speeds of both vehicles are maintained at about 40 km/h. To calculate the stationary distance, a threshold need to be selected at first. Considering the simulated results should compare with the measurement data in [48], so we chose the same threshold 0.8 for both LOS and NLOS scenarios as [48]. In Fig. 8, it can be clearly found that the stationary distance of the NLOS scenario is smaller than that of LOS, because the

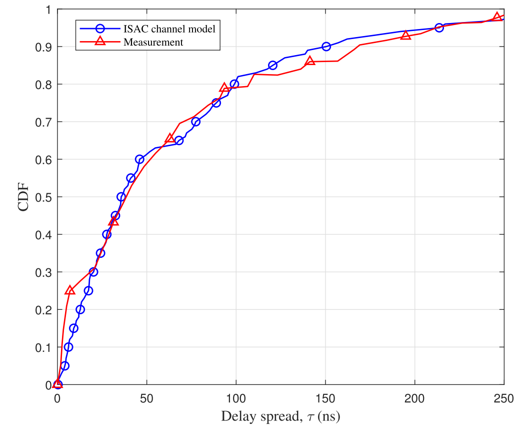

(a) Urban scenarios

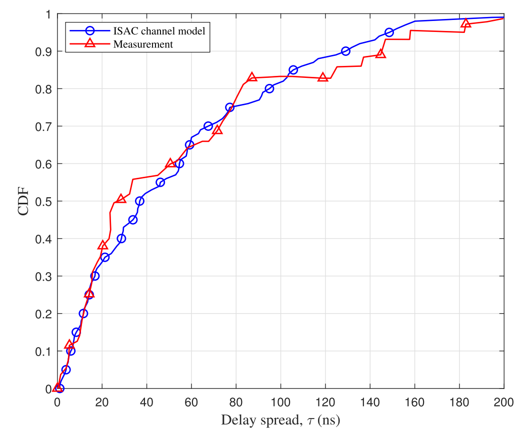

(b) Suburban scenarios

Fig. 7. The comparison of RMS DSs of the proposed ISAC channel model and measurement data in [47] (a) urban scenarios and (b) suburban scenarios (f_c = 5.9 GHz, D = 30 m, M_T = 1, M_R^c = 16, $\delta^T = \delta_C^R = \lambda/2$, $\beta_A^T = \pi/6$, $\beta_E^T = 0$, $\beta_A^R = \pi/6$, $\beta_E^R = 0$, $v^{A_n}(t) = v^{A_l}(t) = v^{Z_n}(t) = v^{Z_l}(t) =$ 0 m/s, $\alpha_A^R(t) = \alpha_E^R(t) = 0$, (a) v^R = 17 m/s, $\sigma_A^T = 39°$, $\sigma_E^T = 5°$, $\sigma_A^R = 38.57°$, $\sigma_E^R = 5.99°$, (b) v^R = 11 m/s, $\sigma_A^T = 29°$, $\sigma_E^T = 15°$, $\sigma_A^R = 25.38°$, $\sigma_E^R = 13.71°$).

LOS path is relatively stable and the power of the LOS path is large, a similar conclusion is also drawn in [49]. Moreover, the simulation results in Fig. 8 and the measurement data align well with each other, which proves the practicability of the proposed channel model.

G. Coherence Bandwidth

The 90% and 50% coherence bandwidths can be obtained when the values of c_{th} in (57) are 0.9 and 0.5, respectively. The cumulative distribution functions (CDFs) of 90% and 50% coherence bandwidth simulation results of the proposed ISAC channel model and measurement data in [50] are compared in Fig. 9. The measurements in [50] were conducted at 5.9 GHz in a suburban scenario with two lanes, the width of the lanes is about 8 to 10 m. There are some trees and buildings on both sides of the street with distances of 10 to 12 m. Tx and Rx did not pass through each other during the measurement. Fig. 9 shows that the CDFs of 90% and 50%

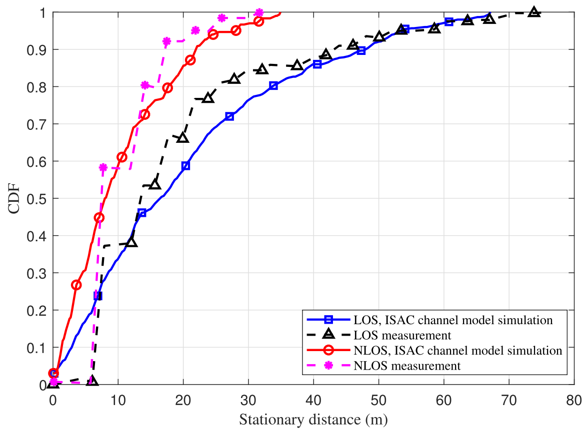

Fig. 8. The comparison of stationary distances of the proposed ISAC channel model and measurement data in [48] (f_c = 5.9 GHz, D = 150 m, M_T = 1, M_R^c = 16, $\delta^T = \delta_C^R = \lambda/2$, $\beta_A^T = \pi/2$, $\beta_E^T = 0$, $\beta_A^R = \pi/2$, $\beta_E^R = 0$, v^R = 17 m/s, $\alpha_A^R(t) = \alpha_E^R(t) = 0$, $v^{A_n}(t) = v^{A_l}(t) = v^{Z_n}(t) = v^{Z_l}(t)$ = 1 m/s, $\alpha_A^{A_n}(t) = \alpha_A^{A_l}(t) = \pi/2$, $\alpha_E^{A_n}(t) = \alpha_E^{A_l}(t) = 0$, $\alpha_A^{Z_n}(t) = \alpha_A^{Z_l}(t) = \pi/2$, $\alpha_E^{Z_n}(t) = \alpha_E^{Z_l}(t) = 0$, σ_A^T = 27.45°, σ_E^T = 11.5°, σ_A^R = 15.3°, σ_E^R = 7.2° in LOS, σ_A^T = 37.5°, σ_E^T = 13.5°, σ_A^R = 35.1°, σ_E^R = 8.45° in NLOS).

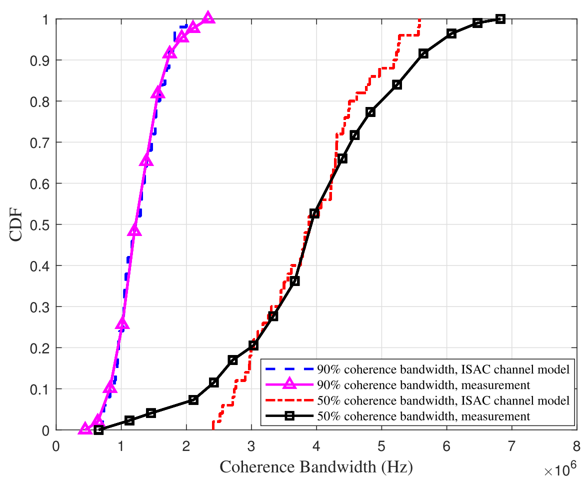

Fig. 9. The comparison of CDFs of 90% and 50% coherence bandwidth of the proposed ISAC channel model and measurement data in [50] (f_c = 5.9 GHz, D = 50 m, M_T = 8, M_R^c = 8, $\delta^T = \delta_C^R = \lambda/2$, $\beta_A^T = \pi/3$, $\beta_E^T = \pi/6$, $\beta_A^R = \pi/3$, $\beta_E^R = \pi/6$, v^R = 20 m/s, $\alpha_A^R(t) = \alpha_E^R(t) = 0$, $v^{A_n}(t) = v^{A_l}(t) = v^{Z_n}(t) = v^{Z_l}(t)$ = 0 m/s, σ_A^T = 44°, σ_E^T = 20.5°, σ_A^R = 35.8°, σ_E^R = 35.2°).

coherence bandwidth simulation results of the ISAC channel model accord well with the measurement results, illustrating the validity of the proposed channel model. According to the measurement results in [50], it can be calculated that the mean values of 90% and 50% coherence bandwidth are about 1.34 MHz and 4.1 MHz, respectively. The mean values of coherence bandwidth obtained from the simulation results are about 1.31 MHz and 3.9 MHz, which proves the accuracy of the proposed channel model.

V. Conclusion

In this paper, a novel 6G ISAC channel model combining forward and backward scattering has been proposed. The characteristics of sensing channel such as the forward scattering and backward scattering have been introduced into the communication channel. Three components, including LOS, forward scattering, and backward scattering, have been summed in a probability weighted way to form a novel communication channel model. Considering the correlations between communication and sensing channels, the information obtained from the sensing channel has been used for more accurate communication channel modeling, reflecting sensing assisted communications. Based on the proposed channel model, statistical characteristics have been derived and simulated, including spatial CCF, temporal ACF, local temporal-Doppler PSD, RMS DS, local Doppler spread, stationary distance, and coherence bandwidth. The analytical results, simulated results, and measurement data match well with each other, demonstrating the validity of the proposed ISAC channel model. As the first ISAC channel model considering both sensing and communications, it is valuable for the design of beamforming and beam tracking algorithms of ISAC systems.

References

[1] C.-X. Wang et al., "On the road to 6G: Visions, requirements, key technologies and testbeds," *IEEE Commun. Surveys Tuts.*, early access, Feb. 27, 2023, doi: 10.1109/COMST.2023.3249835.

[2] C.-X. Wang, J. Huang, H. Wang, X. Gao, X. You, and Y. Hao, "6G wireless channel measurements and models: Trends and challenges," *IEEE Veh. Technol. Mag.*, vol. 15, no. 4, pp. 22–32, Dec. 2020.

[3] W. Jiang, B. Han, M. A. Habibi, and H. D. Schotten, "The road towards 6G: A comprehensive survey," *IEEE Open J. Commun. Soc.*, vol. 2, pp. 334–366, 2021.

[4] M. Wang, Y. Lin, Q. Tian, and G. Si, "Transfer learning promotes 6G wireless communications: Recent advances and future challenges," *IEEE Trans. Rel.*, vol. 70, no. 2, pp. 790–807, Jun. 2021.

[5] F. Liu, C. Masouros, A. P. Petropulu, H. Griffiths, and L. Hanzo, "Joint radar and communication design: Applications, state-of-the-art, and the road ahead," *IEEE Trans. Commun.*, vol. 68, no. 6, pp. 3834–3862, Jun. 2020.

[6] F. Hessar and S. Roy, "Spectrum sharing between a surveillance radar and secondary Wi-Fi networks," *IEEE Trans. Aerosp. Electron. Syst.*, vol. 52, no. 3, pp. 1434–1448, Jun. 2016.

[7] C. De Lima et al., "Convergent communication, sensing and localization in 6G systems: An overview of technologies, opportunities and challenges," *IEEE Access*, vol. 9, pp. 26902–26925, 2021.

[8] W. Saad, M. Bennis, and M. Chen, "A vision of 6G wireless systems: Applications, trends, technologies, and open research problems," *IEEE Netw.*, vol. 34, no. 3, pp. 134–142, May/Jun. 2019.

[9] T. S. Rappaport et al., "Wireless communications and applications above 100 GHz: Opportunities and challenges for 6G and beyond," *IEEE Access*, vol. 7, pp. 78729–78757, 2019.

[10] C.-X. Wang, J. Bian, J. Sun, W. Zhang, and M. Zhang, "A survey of 5G channel measurements and models," *IEEE Commun. Surveys Tuts.*, vol. 20, no. 4, pp. 3142–3168, 4th Quart., 2018.

[11] C.-X. Wang, J. Wang, S. Hu, Z. Jiang, J. Tao, and F. Yan, "Key technologies in 6G terahertz wireless communication systems: A survey," *IEEE Veh. Technol. Mag.*, vol. 16, no. 4, pp. 27–37, Dec. 2021.

[12] C.-X. Wang, Z. Lv, X. Gao, X. You, Y. Hao, and H. Haas, "Pervasive wireless channel modeling theory and applications to 6G GBSMs for all frequency bands and all scenarios," *IEEE Trans. Veh. Technol.*, vol. 71, no. 9, pp. 9159–9173, Sep. 2022.

[13] J. Huang et al., "Reconfigurable intelligent surfaces: Channel characterization and modeling," *Proc. IEEE*, vol. 110, no. 9, pp. 1290–1311, Sep. 2022.

[14] L. Zheng, M. Lops, Y. C. Eldar, and X. Wang, "Radar and communication coexistence: An overview: A review of recent methods," *IEEE Signal Process. Mag.*, vol. 36, no. 5, pp. 85–99, Sep. 2019.

[15] O. B. Akan and M. Arik, "Internet of Radars: Sensing versus sending with joint radar-communications," *IEEE Commun. Mag.*, vol. 58, no. 9, pp. 13–19, Sep. 2020.

[16] B. Paul, A. R. Chiriyath, and D. W. Bliss, "Survey of RF communications and sensing convergence research," *IEEE Access*, vol. 5, pp. 252–270, 2017.

[17] A. Zhang, M. L. Rahman, X. Huang, Y. J. Guo, S. Chen, and R. W. Heath Jr., "Perceptive mobile networks: Cellular networks with radio vision via joint communication and radar sensing," *IEEE Veh. Technol. Mag.*, vol. 16, no. 2, pp. 20–30, Jun. 2021.

[18] A. R. Chiriyath, B. Paul, and D. W. Bliss, "Radar-communications convergence: Coexistence, cooperation, and co-design," *IEEE Trans. Cogn. Commun. Netw.*, vol. 3, no. 1, pp. 1–12, Mar. 2017.

[19] Z. Feng, Z. Fang, Z. Wei, X. Chen, Z. Quan, and D. Ji, "Joint radar and communication: A survey," *China Commun.*, vol. 17, no. 1, pp. 1–27, Jan. 2020.

[20] C. B. Barneto et al., "Full-duplex OFDM radar with LTE and 5G NR waveforms: Challenges, solutions, and measurements," *IEEE Trans. Microw. Theory Techn.*, vol. 67, no. 10, pp. 4042–4054, Oct. 2019.

[21] F. Liu et al., "Integrated sensing and communications: Towards dual-functional wireless networks for 6G and beyond," *IEEE J. Sel. Areas Commun.*, vol. 40, no. 6, pp. 1728–1767, Jun. 2022.

[22] M. Alaee-Kerharoodi, S. M. R. Bhavani, K. V. Mishra, and B. Ottersten, "Information theoretic approach for waveform design in coexisting MIMO radar and MIMO communications," in *Proc. IEEE ICASSP*, Barcelona, Spain, May 2020, pp. 1–5.

[23] Y. Cui, F. Liu, X. Jing, and J. Mu, "Integrating sensing and communications for ubiquitous IoT: Applications, trends, and challenges," *IEEE Netw.*, vol. 35, no. 5, pp. 158–167, Sep./Oct. 2021.

[24] S. D. Liyanaarachchi, T. Riihonen, C. B. Barneto, and M. Valkama, "Optimized waveforms for 5G–6G communication with sensing: Theory, simulations and experiments," *IEEE Trans. Wireless Commun.*, vol. 20, no. 12, pp. 8301–8315, Dec. 2021.

[25] F. Liu, Y.-F. Liu, A. Li, C. Masouros, and Y. C. Eldar, "Cramér–Rao bound optimization for joint radar-communication beamforming," *IEEE Trans. Signal Process.*, vol. 70, pp. 240–253, 2022.

[26] P. Kumari, J. Choi, N. González-Prelcic, and R. W. Heath Jr., "IEEE 802.11ad-based radar: An approach to joint vehicular communication-radar system," *IEEE Trans. Veh. Technol.*, vol. 67, no. 4, pp. 3012–3027, Apr. 2018.

[27] K. V. Mishra, M. R. B. Shankar, V. Koivunen, B. Ottersten, and S. A. Vorobyov, "Toward millimeter-Wave joint radar communications: A signal processing perspective," *IEEE Signal Process. Mag.*, vol. 36, no. 5, pp. 100–114, Sep. 2019.

[28] F. Liu and C. Masouros, "A tutorial on joint radar and communication transmission for vehicular networks—Part II: State of the art and challenges ahead," *IEEE Commun. Lett.*, vol. 25, no. 2, pp. 327–331, Feb. 2021.

[29] F. Liu and C. Masouros, "A tutorial on joint radar and communication transmission for vehicular networks—Part III: Predictive beamforming without state models," *IEEE Commun. Lett.*, vol. 25, no. 2, pp. 332–336, Feb. 2021.

[30] S. H. Dokhanchi, M. R. B. Shankar, K. V. Mishra, and B. Ottersten, "Multi-constraint spectral co-design for colocated MIMO radar and MIMO communications," in *Proc. ICASSP*, Barcelona, Spain, May 2020, pp. 4567–4571.

[31] D. Ma, N. Shlezinger, T. Huang, Y. Liu, and Y. C. Eldar, "Joint radar-communication strategies for autonomous vehicles: Combining two key automotive technologies," *IEEE Signal Process. Mag.*, vol. 37, no. 4, pp. 85–97, Jul. 2020.

[32] A. Herschfelt, A. Chiriyath, D. W. Bliss, C. D. Richmond, U. Mitra, and S. D. Blunt, "Vehicular RF convergence: Simultaneous radar, communications, and PNT for urban air mobility and automotive applications," in *Proc. IEEE Radar Conf. (RadarConf)*, Florence, Italy, Sep. 2020, pp. 1–6.

[33] L. Gaudio, M. Kobayashi, G. Caire, and G. Colavolpe, "On the effectiveness of OTFS for joint radar parameter estimation and communication," *IEEE Trans. Wireless Commun.*, vol. 19, no. 9, pp. 5951–5965, Sep. 2020.

[34] B. Xiong, Z. Zhang, J. Zhang, H. Jiang, J. Dang, and L. Wu, "Novel multi-mobility V2X channel model in the presence of randomly moving clusters," *IEEE Trans. Wireless Commun.*, vol. 20, no. 5, pp. 3180–3195, May 2021.

[35] S. Wu, C.-X. Wang, E.-H. M. Aggoune, M. M. Alwakeel, and X. You, "A general 3-D non-stationary 5G wireless channel model," *IEEE Trans. Commun.*, vol. 66, no. 7, pp. 3065–3078, Jul. 2018.

[36] J. Bian et al., "A WINNER+ based 3-D non-stationary wideband MIMO channel model," *IEEE Trans. Wireless Commun.*, vol. 17, no. 3, pp. 1755–1767, Mar. 2018.

[37] H. Jiang, Z. Zhang, L. Wu, and J. Dang, "A non-stationary geometry-based scattering vehicle-to-vehicle MIMO channel model," *IEEE Commun. Lett.*, vol. 22, no. 7, pp. 1510–1513, Jul. 2018.

[38] J. Bian, C.-X. Wang, X. Q. Gao, X. You, and M. Zhang, "A general 3D non-stationary wireless channel model for 5G and beyond," *IEEE Trans. Wireless Commun.*, vol. 20, no. 5, pp. 3211–3224, May 2021.

[39] A. Freeman and S. L. Durden, "A three-component scattering model for polarimetric SAR data," *IEEE Trans. Geosci. Remote Sens.*, vol. 36, no. 3, pp. 963–973, May 1998.

[40] R. Verdone and A. Zanella, *Pervasive Mobile and Ambient Wireless Communications*. London, U.K.: Springer, 2012.

[41] *Study on Channel Model for Frequencies From 0.5 to 100 GHz (Release 14)*, document 3GPP TR 38.901, Version 14.0.0, Mar. 2017.

[42] B. Boashash, "Estimating and interpreting the instantaneous frequency of a signal. I. Fundamentals," *Proc. IEEE*, vol. 80, no. 4, pp. 520–538, Apr. 1992.

[43] B. Chen, Z. Zhong, and B. Ai, "Stationarity intervals of time-variant channel in high speed railway scenario," *China Commun.*, vol. 9, no. 8, pp. 64–70, Aug. 2012.

[44] J. Bian, C.-X. Wang, Y. Liu, J. Tian, J. Qiao, and X. Zheng, "3D non-stationary wideband UAV-to-ground MIMO channel models based on aeronautic random mobility model," *IEEE Trans. Veh. Technol.*, vol. 70, no. 11, pp. 11154–11168, Nov. 2021.

[45] J. Li et al., "Channel characterization for massive MIMO in subway station environment at 6 GHz and 11 GHz," in *Proc. VTC-Fall*, Chicago, IL, USA, Aug. 2018, pp. 1–5.

[46] L. Cheng, B. Henty, F. Bai, and D. D. Stancil, "Doppler spread and coherence time of rural and highway vehicle-to-vehicle channels at 5.9 GHz," in *Proc. IEEE GLOBECOM*, New Orleans, LA, USA, Nov./Dec. 2008, pp. 1–6.

[47] M. Yang et al., "A cluster-based 3D channel model for vehicle-to-vehicle communications," in *Proc. IEEE/CIC ICCC*, Beijing, China, Aug. 2018, pp. 741–746.

[48] M. Yang et al., "Measurements and cluster-based modeling of vehicle-to-vehicle channels with large vehicle obstructions," *IEEE Trans. Wireless Commun.*, vol. 19, no. 9, pp. 5860–5874, Sep. 2020.

[49] Q. Wang, D. W. Matolak, and B. Ai, "Shadowing characterization for 5-GHz vehicle-to-vehicle channels," *IEEE Trans. Veh. Technol.*, vol. 67, no. 3, pp. 1855–1866, Mar. 2018.

[50] L. Cheng, B. Henty, R. Cooper, D. D. Stancil, and F. Bai, "Multi-path propagation measurements for vehicular networks at 5.9 GHz," in *Proc. IEEE WCNC*, Las Vegas, NV, USA, Mar. 2008, pp. 1239–1244.

Runruo Yang (Student Member, IEEE) received the B.E. degree in information and communication engineering from the University of Electronic Science and Technology of China, in 2018. She is currently pursuing the Ph.D. degree with the National Mobile Communications Research Laboratory, Southeast University, China. Her research interests are massive MIMO wireless channel measurements and modeling, integrated sensing, communication channel measurements, and modeling.

Cheng-Xiang Wang (Fellow, IEEE) received the B.Sc. and M.Eng. degrees in communication and information systems from Shandong University, Jinan, China, in 1997 and 2000, respectively, and the Ph.D. degree in wireless communications from Aalborg University, Aalborg, Denmark, in 2004.

He was a Research Assistant with the Hamburg University of Technology, Hamburg, Germany, from 2000 to 2001; a Visiting Researcher with Siemens AG Mobile Phones, Munich, Germany, in 2004; and a Research Fellow with the University of Agder, Grimstad, Norway, from 2001 to 2005. He has been with Heriot-Watt University, Edinburgh, U.K., since 2005, where he was promoted to a Professor in 2011. In 2018, he joined Southeast University, Nanjing, China, as a Professor. He is also a part-time Professor with the Purple Mountain Laboratories, Nanjing. He has authored four books, three book chapters, and more than 500 papers in refereed journals and conference proceedings, including 27 highly cited papers. He has also delivered 24 invited keynote speeches/talks and 15 tutorials in international conferences. His current research interests include wireless channel measurements and modeling, 6G wireless communication networks, and electromagnetic information theory.

Dr. Wang is a member of the Academia Europaea (The Academy of Europe) and the European Academy of Sciences and Arts (EASA); and a fellow of the Royal Society of Edinburgh (FRSE), IET, and the China Institute of Communications (CIC). He has served as a TPC member, the TPC chair, and the general chair for more than 80 international conferences. He received 15 Best Paper Awards from IEEE GLOBECOM 2010, IEEE ICCT 2011, ITST 2012, IEEE VTC 2013-Spring, IWCMC 2015, IWCMC 2016, IEEE/CIC ICCC 2016, WPMC 2016, WOCC 2019, IWCMC 2020, WCSP 2020, CSPS 2021, WCSP 2021, and IEEE/CIC ICCC 2022. He was a Highly-Cited Researcher recognized by Clarivate Analytics in 2017–2020. He is currently an Executive Editorial Committee Member of the IEEE TRANSACTIONS ON WIRELESS COMMUNICATIONS. He has served as an Editor for over ten international journals, including the IEEE TRANSACTIONS ON WIRELESS COMMUNICATIONS, from 2007 to 2009, the IEEE TRANSACTIONS ON VEHICULAR TECHNOLOGY, from 2011 to 2017, and the IEEE TRANSACTIONS ON COMMUNICATIONS, from 2015 to 2017. He was a Guest Editor of the IEEE JOURNAL ON SELECTED AREAS IN COMMUNICATIONS, Special Issue on Vehicular Communications and Networks (Lead Guest Editor), Special Issue on Spectrum and Energy Efficient Design of Wireless Communication Networks, and Special Issue on Airborne Communication Networks. He was also a Guest Editor of the IEEE TRANSACTIONS ON BIG DATA, Special Issue on Wireless Big Data. He is a Guest Editor of the IEEE TRANSACTIONS ON COGNITIVE COMMUNICATIONS AND NETWORKING, Special Issue on Intelligent Resource Management for 5G and Beyond. He was an IEEE Communications Society Distinguished Lecturer in 2019 and 2020.

Jie Huang (Member, IEEE) received the B.E. degree in information engineering from Xidian University, China, in 2013, and the Ph.D. degree in information and communication engineering from Shandong University, China, in 2018. From October 2018 to October 2020, he was a Post-Doctoral Research Associate with the National Mobile Communications Research Laboratory, Southeast University, China, supported by the National Post-Doctoral Program for Innovative Talents. From January 2019 to February 2020, he was a Post-Doctoral Research Associate with Durham University, U.K. Since March 2019, he is a part-time Researcher with the Purple Mountain Laboratories, China. Since November 2020, he has been an Associate Professor with the National Mobile Communications Research Laboratory, Southeast University. He has authored and coauthored more than 70 papers in refereed journals and conference proceedings. His research interests include millimeter wave, massive MIMO, reconfigurable intelligent surface channel measurements and modeling, wireless big data, and 6G wireless communications. He received the Best Paper Awards from WPMC 2016, WCSP 2020, and WCSP 2021. He has delivered eight tutorials in IEEE/CIC ICCC 2021, IEEE PIMRC 2021, IEEE ICC 2022, IEEE VTC-Spring 2022, IEEE/CIC ICCC 2022, IEEE VTC-Fall 2022, IEEE PIMRC 2022, and IEEE Globecom 2022.

El-Hadi M. Aggoune (Life Senior Member, IEEE) received the M.S. and Ph.D. degrees in electrical engineering from the University of Washington (UW), Seattle, WA, USA. He served at several universities in the U.S. and abroad at many academic ranks including the Endowed Chair Professor. He is currently serving as a Professor and the Director of the Sensor Networks and Cellular Systems (SNCS) Research Center, University of Tabuk. He is listed as a Inventor in several patents, one of them assigned to Boeing Company, USA. He is a Professional Engineer registered in the state of Washington. He has coauthored papers in IEEE and other journals and conferences, and served on editorial boards and technical committees for many of them. He was a recipient of the IEEE Professor of the Year Award, UW. He was the Director of a laboratory that received the Boeing Supplier Excellence Award. His research interests include wireless communication, sensor networks, power systems, neurocomputing, and scientific visualization.

Yang Hao (Fellow, IEEE) received the Ph.D. degree in computational electromagnetics from the Centre for Communications Research, University of Bristol, Bristol, U.K., in 1998.

He was a Post-Doctoral Research Fellow with the School of Electronic, Electrical and Computer Engineering, University of Birmingham, Birmingham, U.K. He is currently a Professor of antennas and electromagnetics with the Antenna Engineering Group, Queen Mary University of London, London, U.K. He developed several fully integrated antenna solutions based on novel artificial materials to reduce mutual RF interference, weight, cost, and system complexity for security, aerospace, and healthcare, with leading U.K. industries, and novel and emergent gradient index materials to reduce mass, footprint, and profile of low-frequency and broadband antennas. He also co-developed the first stable active non-Foster metamaterial to enhance usability through small antenna size, high directivity, and tuneable operational frequency. He coined the term body-centric wireless communications, i.e., networking among wearable and implantable wireless sensors on the human body. He was the first to characterize and include the human body as a communication medium between on-body sensors using surface and creeping waves. He contributed to the industrial development of the first wireless sensors for healthcare monitoring. He has authored or coauthored more than 200 journal articles and has co-edited and coauthored the books textitAntennas and Radio Propagation for Body-Centric Wireless Communications (Artech House, 2006 and 2012) and textitFDTD Modeling of Metamaterials: Theory and Applications (Artech House, 2008), respectively. His current research interests include computational electromagnetics, microwave metamaterials, graphene and nanomicrowaves, antennas and radio propagation for bodycentric wireless networks, active antennas for millimeter/submillimeter applications, and photonic integrated antennas.

Dr. Hao is an elected fellow of Royal Academy of Engineering and IET. He won the 2015 IET AF Harvey Research Prize and was a co-recipient of the BAE Chairmans Silver Award in 2014 and the Royal Society Wolfson Research Merit Award.